Remote Sensing of Environment 247 (2020) 111927

Contents lists available at ScienceDirect

Remote Sensing of Environment

journal homepage: www.elsevier.com/locate/rse

Remote sensing spatiotemporal patterns of frozen soil and the environmental controls over the Tibetan Plateau during 2002–2016

Guanheng Zheng[a,b], Yuting Yang[a], Dawen Yang[a,*], Baptiste Dafflon[b], Yonghong Yi[c], Shulei Zhang[d], Deliang Chen[e], Bing Gao[f], Taihua Wang[a], Ruijie Shi[a], Qingbai Wu[g]

[a] State Key Laboratory of Hydroscience and Engineering, Department of Hydraulic Engineering, Tsinghua University, Beijing 100084, China
[b] Lawrence Berkeley National Laboratory, 1 Cyclotron Rd., Berkeley, CA 94720, United States
[c] Jet Propulsion Laboratory, California Institute of Technology, Pasadena, CA, USA
[d] State Key Laboratory of Earth Surface Process and Resource Ecology, School of Natural Resources, Faculty of Geographical Science, Beijing Normal University, Beijing, China
[e] Regional Climate Group, Department of Earth Sciences, University of Gothenburg, Gothenburg, Sweden
[f] School of Water Resources and Environment, China University of Geosciences, Beijing 100083, China
[g] Northwest Institute of Eco-environment and Resource, Chinese Academy of Sciences, Lanzhou 730000, China

ARTICLE INFO

Keywords:
Frozen soil
Seasonally frozen ground
Permafrost
Spatiotemporal patterns
Climatic controls
Satellite remote sensing
Process-based model
Tibetan plateau

ABSTRACT

The changing climate is affecting the frozen soil at an unprecedented rate across the Northern Hemisphere. However, due to sparse ground measurements, the changes of frozen soil and the environmental controls over the vast cryosphere are still unclear, such as in the Tibetan Plateau (TP). In this study, a process-based model solely driven by satellite remote sensing data is employed to investigate the spatiotemporal changes of seasonally frozen ground and permafrost over the entire TP (~3 million km^2) during 2002–2016 at a spatial resolution of 1 km. Comprehensive validations against in situ observations of frozen ground types, mean annual ground temperature, active layer thickness, soil temperature, and frozen depth at 608 boreholes and 109 meteorological stations demonstrate an overall satisfactory performance of the model in reproducing the spatial pattern and temporal evolution of the frozen soil in the region. Spatially, land surface temperature (LST; both in-season and off-season) primarily controls the frozen ground types and frozen depth, with seasonally frozen ground and permafrost covering ~56% and ~ 37% of the plateau, respectively. The estimated spatial-averaged annual maximum soil freeze depth (SFD) is ~1.29 m, and the annual maximum active layer thickness (ALT) of permafrost is ~1.85 m. Temporally, ALT shows an overall increasing trend at an average rate of +3.17 cm yr^{-1}, while SFD exhibits both decreasing (at ~62% areas) and increasing (at ~38% areas) trends in the region. Again, LST is found to be the dominant factor that controls the temporal changes in both SFD and ALT while precipitation (i.e., both rainfall and snowfall) plays an important (especially in more arid areas and regions near the lower limit of permafrost) but secondary role. Our results demonstrate the advantages of the satellite-based method in frozen soil simulations over large scales with complex topography and landscape and highlight the important roles of both temperature and precipitation in shaping the frozen soil patterns on the TP or other cold, dry regions.

1. Introduction

Frozen soil, including the seasonally frozen ground and permafrost, occupies more than 50% of the exposed land surface in the Northern Hemisphere (Zhang et al., 1999). The freezing/thawing processes periodically change the hydrothermal properties of ground soil, which exert influences on the lower atmosphere (Slater et al., 1998; Cheng and Wu, 2007), hydrological cycle (Wang, 1990; Wang et al., 2009), and ecosystem functioning (Grosse et al., 2016). Over the past decades, climate change, characterized by persistent warming, has incurred large impacts on the global cryosphere, including the Tibetan Plateau (TP) (Biskaborn et al., 2019; Cheng and Wu, 2007; Ding et al., 2019). Observations have indicated considerable degradations of permafrost and seasonally frozen ground on the TP since the 1980s (Wu and Zhang, 2010; Wu et al., 2015). The degradation of frozen soil is further accompanied with other environmental issues, such as the decline of

* Corresponding author.
E-mail address: yangdw@tsinghua.edu.cn (D. Yang).

https://doi.org/10.1016/j.rse.2020.111927
Received 29 October 2019; Received in revised form 28 May 2020; Accepted 29 May 2020

water table, the drying of near-surface soil, and the reduction in soil carbon and nitrogen stocks (Baumann et al., 2009; Zhang et al., 2004; Zhou et al., 2000). In this light, a better understanding of the spatial and temporal changes of frozen soil and the driving mechanisms is imperative to achieve sustainable water and ecosystem management over the plateau region (Karjalainen et al., 2019).

Due to the harsh environment and complex landscape, in situ observations of frozen soil on the TP are extremely limited, which precludes the understanding of frozen soil distributions and changes over the entire plateau (Wang et al., 2006; Wu and Zhang, 2010; Wu et al., 2013; Yang et al., 2008). In comparison, satellite remote sensing provides an unprecedented opportunity to monitor the spatially continuous land surface information across large geographic extents, which has been proven to be a useful tool for monitoring frozen soil across the globe (Brucker et al., 2014; Li et al., 2015; Kim et al., 2017; Obu et al., 2019; Roy et al., 2015; Rautiainen et al., 2016). Compared with Interferometric Synthetic-Aperture Radar (InSAR) that usually has a coarse temporal resolution (typically longer than 5 d; Bianchini et al., 2018) and passive microwave remote sensing that often contains a coarse spatial resolution (typically coarser than 10 km; Lyu et al., 2018), the thermal-band remote sensing data has both shorter temporal intervals and finer spatial resolutions (e.g., 1 km and 12 h for MODIS land surface temperature; LST) that are more appropriate for capturing fine-scale variations of frozen soil properties in mountainous regions and has hence attracted increasing research interests in recent years (Ran and Li, 2019; Zheng et al., 2019). For example, remotely-sensed LST has been incorporated into statistical/empirical and process-based models to retrieve frozen soil properties (e.g., ground temperature, permafrost area, seasonally frozen depth, and active layer thickness) in many previous studies and obtained reasonable accuracies (Langer et al., 2013; Obu et al., 2019; Shi et al., 2018; Westermann et al., 2015; Zou et al., 2017; Yi et al., 2018, 2019; Zheng et al., 2019). Compared with statistical/empirical methods, which are generally more computationally efficient, process-based models have a more solid physical base and are able to simulate key relevant processes (Karjalainen et al., 2019; Wu et al., 2018). Additionally, process-based models are less contingent on ground observations for model calibration and thus often have a better transferability to different regions (e.g., Peng et al. (2017) vs Gao et al. (2018)).

In a previous study, Zheng et al. (2019) proposed a fully remote sensing-driven, process-based model for frozen soil simulation (i.e., geomorphology based ecohydrological model-remote sensing, GBEHM-RS) and tested the model in a mountainous region (~10^5 km^2) in the northeast TP. This study will extend the study of Zheng et al. (2019) to the entire TP (~10^6 km^2), which features a strong elevation gradient and expands over multiple climatic (i.e., arid, semi-arid, sub-humid, and humid) and ecological (i.e., forest, shrubland, grassland, alpine meadow, and desert) zones. Compared with other remote sensing-based models developed for the pan-arctic region (e.g., Langer et al., 2013; Yi et al., 2018), GBEHM-RS is superior in its ability to couple soil water-heat dynamics (Zheng et al., 2019), which is essential for regions where soil moisture presents large variations both through time and across space (Westermann et al., 2016), and might be more suitable for regions with complex climate and landscape, such as the TP. Additionally, Zheng et al. (2019) mainly evaluated the performance of GBEHM-RS over seasonally frozen ground. However, the model performance in simulating permafrost and temporal frozen soil changes are still not validated.

In addition to knowledge on the spatial and temporal patterns of frozen soil, it is also of great importance to understand the driving factors that lead to these patterns (Karjalainen et al., 2019; Smith and Riseborough, 2002). In theory, frozen soil conditions are primarily affected by large-scale climatic forcings (i.e., precipitation and temperature) and mediated by several local factors (e.g., vegetation, topography, and soil texture) (Ding et al., 2019; Shur and Jorgenson, 2007; Wu et al., 2015; Yang et al., 2008; Yin et al., 2017). In terms of the spatial patterns, temperature and precipitation dominantly control long-term heat and water distributions that determine the large-scale distributions of ground thermal regimes (e.g., Westermann et al., 2015), while local factors add further fine-scale heterogeneities to frozen soil distribution (Karjalainen et al., 2019). On the one hand, temperature is directly linked with ground thermal status; on the other hand, precipitation, both as rainfall (P_{liquid}) and snowfall (P_{solid}), impacts on the soil freezing/thawing processes through changing soil water movement (Kane et al., 2002; Luthin and Guymon, 1974), changing soil thermal properties (e.g., phase-change heat, heat capacity, and thermal conductivities; Hinkel et al., 2001; Wen et al., 2014), and mediating the heat exchange between the land and the atmosphere due to the insulation effect of the snow layer (Hardy et al., 2001; Stieglitz et al., 2003; Yang et al., 2008; Zhang, 2005), respectively. For temporal changes, changes in climate conditions are presumably the only factors that could lead to evident changes in frozen soil (Ran et al., 2018), as topography and soil texture are generally stable at the climatic time scale and vegetation often co-varies with climate (Zhong et al., 2010). Unfortunately, despite its importance for predicting future frozen soil conditions under climate change, the driving mechanisms underlying the spatial and temporal dynamics of frozen soil over the TP region is still largely unknown.

Therefore, the objectives of this study were to (i) apply GBEHM-RS to simulate frozen soil across the entire TP and comprehensively evaluate the model performance in the region, (ii) map the spatial patterns of frozen soil over the TP and identify the relative importance of relevant drivers leading to these patterns, and (iii) examine the temporal changes of frozen soil over the TP during 2002–2016 and quantify the contributions of the controlling factors.

2. Study area and data

2.1. Study area

The TP region with an elevation higher than 2000 m a.s.l (see Fig. 1) is our study area, which locates between 70°–105°E and 25°–40°N and covers a total area of 3.35 million km^2 (including the glaciers and lakes). The TP has a typical cold and semiarid climate and a complex landscape (Supplementary Figs. S1 and S2; Lu et al., 2017). From southeast to northwest, the vegetation type changes from shrub, alpine meadow/grassland, to alpine steppe/desert (Feng et al., 2019), the mean annual LST decreases from +15 °C to −11 °C, and the mean annual precipitation decreases from over 1700 mm to less than 50 mm (Tong et al., 2014). For precipitation, P_{liquid} compromises ~60% of the total precipitation and is mainly concentrated in the southeast region, whereas P_{solid} primarily occurs in the mountain ranges as well as southern and western margins (Supplementary Fig. S1). In addition, due to the large elevation range (from 2000 m to above 8000 m a.s.l.), the TP is also characterized as a mountainous frozen soil region with the most developed permafrost and seasonally frozen soil in the mid- and low latitudes (Cheng and Wu, 2007).

2.2. Data

2.2.1. Model inputs

Two sets of model input data are used in this study, including satellite-based climatic forcing and substrate land surface properties. The satellite-based climatic forcing includes LST, precipitation, cloud fraction, air temperature, relative humidity, and air pressure, which are taken from three satellite sensors including (i) Moderate Resolution Imaging Spectroradiometer (MODIS); (ii) Atmospheric Infrared Sounder (AIRS); and (iii) Tropical Rainfall Measuring Mission (TRMM). The second model input dataset consists of topography, vegetation parameter (i.e., normalized difference vegetation index, NDVI), surface albedo, soil parameters (i.e., bulk density and weighted percent of sand, clay, soil organic matter, and gravel), and snow cover that describe the

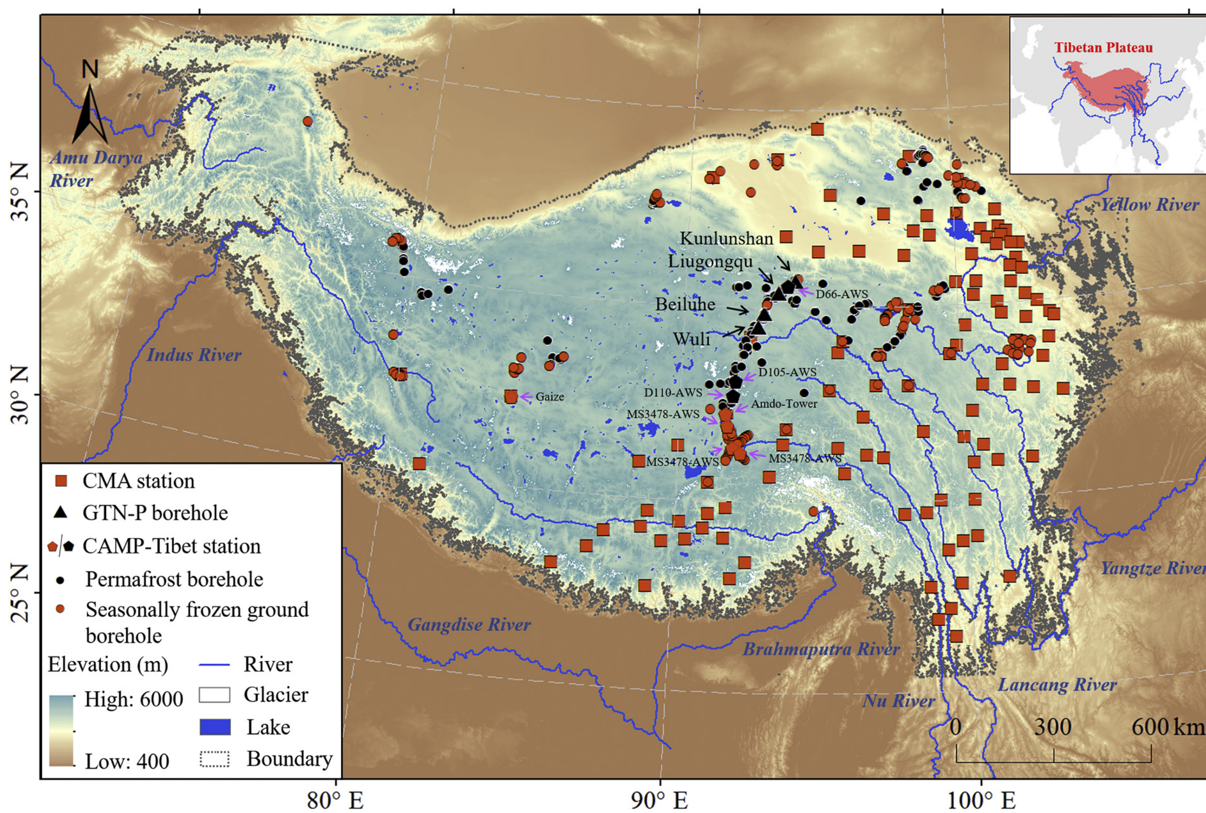

Fig. 1. Locations of the study area and the observational sites. Symbols in red represent seasonally frozen ground and those in black represent permafrost. The China Meteorological Administration (CMA) meteorological stations are illustrated as solid squares, the Global Terrestrial Network for Permafrost (GTN-P) boreholes are depicted as solid triangles, Coordinated Enhanced Observing Period (CEOP) Asia-Australia Monsoon Project (CAMP) on the Tibetan Plateau (CAMP-Tibet) stations are represented with solid pentagons, and the solid dots represent borehole measurements from other sources (Cao et al., 2019; Jin et al., 2009, 2011; Liu, 2015; Liu et al., 2015; Luo et al., 2012a, 2012b, 2018; Qiao et al., 2015; Wu and Zhang, 2008; Wu et al., 2010, 2015, 2017; Xie et al., 2012, 2015; Zhang et al., 2004). The grey dotted line circles the study area and the background colour depict elevation. (For interpretation of the references to colour in this figure legend, the reader is referred to the web version of this article.)

substrate properties. A detailed description of the datasets is summarized in Table 1 and can be also found in Zheng et al. (2019). All of these data were resampled to a 1-km spatial resolution using the nearest interpolation method.

2.2.2. Ground-based measurements

Ground-based measurements of LST and precipitation were collected at China Meteorological Administration (CMA) stations from 2002 to 2015, and ground-based observations of downward shortwave radiation (SWD), downward longwave radiation (LWD), and surface albedo (α) were collected at Coordinated Enhanced Observing Period (CEOP) Asia-Australia Monsoon Project (CAMP) on the Tibetan Plateau (CAMP-Tibet) stations from 2002 to 2004. It is worthwhile noting that for the total 109 CMA stations within the study region (Fig. 1), only 75 of them have LST and precipitation measurements (referred to as the CMA group 2 stations in Supplementary Fig. S2). At the CMA stations, LST was measured using glass liquid thermometers at four times per day (i.e., 2:00 AM/PM and 8:00 AM/PM, local time) (CMA, 2004), and the average of the four measurements was used to represent daily mean LST. In comparison, SWD, LWD, and α were measured at a higher frequency (i.e., hourly) at the eight CAMP-Tibet stations, despite frequent observation gaps. To eliminate the biases caused by incomplete diurnal observations, only days with 24-h continuous observations were used. Compared with the ground-based measurements, the satellite-based LST and precipitation showed reasonable accuracies in the study region in terms of both spatial and temporal variations, with LST showing a mean bias (calculated using the Eq. [A1] in Appendix A) of -0.26 °C and a root-mean-squared error (RMSE; calculated using the Eq. [A2] in Appendix A) of 4.04 °C, and precipitation having a mean bias of 6.17 mm month^{-1} and an RMSE of 26.64 mm month^{-1} (Supplementary Fig. S3). In terms of SWD, LWD, and α, the satellite data have also obtained an overall good accuracy (SWD: mean bias of -21 W m^{-2}, RMSE of 50 W m^{-2}; LWD: mean bias of 5 W m^{-2}, RMSE of 25 W m^{-2}; α: mean bias of -0.01, RMSE of 0.04) (Supplementary Table S1).

The model performance in frozen soil simulation was evaluated using in situ measurements of frozen ground types (i.e., the permafrost and seasonally frozen ground), active layer thickness (ALT), mean annual ground temperature (MAGT), frozen depth (D_f), and soil temperature (T_{soil}) at different depths below the surface. Measurements of frozen ground types, ALT, MAGT, and deep-ground T_{soil} profiles were collected from previously published literature (Cao et al., 2019; Jin et al., 2009, 2011; Liu, 2015; Liu et al., 2015; Luo et al., 2012a, 2012b, 2018; Qiao et al., 2015; Wu and Zhang, 2008; Wu et al., 2010, 2015, 2017; Xie et al., 2012, 2015; Zhang et al., 2004). In total, 608 boreholes have records of frozen ground types, of which 425 boreholes were located on permafrost and 183 boreholes were distributed on seasonally frozen ground (Fig. 1). On the permafrost, ALT were collected at 76 boreholes located in the eastern plateau (see Supplementary Fig. S4a), MAGT were measured at 150 permafrost boreholes with an observational depth of ~10 m (see Supplementary Fig. S4b) and the deep-ground T_{soil} profiles (from the surface to over 40 m deep) were measured using thermistor strings at four GTN-P boreholes (i.e., Kunlunshan, Beiluhe, Liugongqu, and Wuli; Fig. 1). On the seasonally frozen ground, observations of D_f and T_{soil} during 2004–2015 were available at 109 CMA stations that are primarily distributed on the eastern plateau (Fig. 1). The D_f was measured using a frost tube, whose outer iron cover

Table 1
Detailed information for model inputs.

Type	Variable	Product	RS-type	Temporal resolution	Spatial resolution	Data Process
Climatic forcing	LST	MOD/MYD11A1	Thermal infrared	12 h	1 km	Daily mean is computed as the average of the four observations per day
		AIRX3STD	Microwave	12 h	1°	Used when the thermal infrared images are contaminated by cloud covers
	Precipitation	TRMM 3B42 V7	Microwave, infrared	1 d	0.25°	
	Could fraction, Air temperature, Relative humidity, Air pressure	AIRX3STD	Microwave	12 h	1°	Daily mean is computed as the average of the two observations per day
Substrate properties	Topography	SRTM DEM90	Radar	–	90 m	–
	Soil parameters(including the bulk density and weighted percent of sand, clay, soil organic matter, and gravel)	The Soil Database of China for Land Surface Modelling	–	–	30 arc sec	–
	Soil depth	A Global Depth to Bedrock Dataset for Earth System Modelling	–	–	30 arc sec	–
	Surface albedo	MCD43GF	Visible, near-infrared	8 d	30 arc sec	Every 8-day-composite shares the same value
	NDVI	MOD/MYD13Q1	Visible, near-infrared	16 d	250 m	Every 16-day-composite shares the same value
	Snow cover	MOD10A2	Visible, infrared	8 d	500 m	Every 8-day-composite shares the same value

was anchored underground and the inner rubber tube was filled with distilled water. The inner tube was manually pulled outside to measure the D_f at 8:00 AM each day (CMA, 2004). The T_{soil} was measured at eight depths (i.e., 0.05, 0.1, 0.15, 0.2, 0.4, 0.8, 1.6, and 3.2 m) using the thermistors. Similar to that of LST, the T_{soil} at the top five depths were measured four times a day, whereas the T_{soil} at three bottom layers were only measured once a day (at 2:00 PM) (CMA, 2004).

3. Methods

3.1. The GBEHM-RS

The GBEHM-RS is used to simulate the spatial patterns and temporal changes of frozen soil over the TP during 2002–2016. Here we provide a brief introduction of GEBHM-RS and more details on the model description and its parameterizations can be found in Zheng et al. (2019) and Gao et al. (2018). The GBEHM-RS is a remote sensing version of the geomorphology based ecohydrological model (GBEHM), which is a distributed ecohydrological model designed for simulating the coupled interactions between frozen soil, hydrology, and ecosystem by Yang et al. (2015). In a previous study, Zheng et al. (2019) modified the original GBEHM to allow it (i.e., GBEHM-RS) fully adapt to remote sensing inputs. GBEHM-RS has a coupled parameterization of the heat-water interactions in the soil layer and snowpack. The heat transfer is solved using the equation formulated by Flerchinger and Saxton (1989), the soil water movement is solved based on the Richards equation, and the snow processes (i.e., accumulation, grain aging, compaction, and melting) are parameterized based on the approaches proposed by Anderson (1976), Dai and Zeng (1997), Jordan (1991), and Bartelt and Lehning (2002). For heat transfer, the upper boundary uses the satellite-based LST at the interface between the soil or snow (when existed) and the atmosphere, and the lower boundary adopts a prescribed geothermal flux near the bedrock bottom. The soil water movement is only simulated within the soil layer, where the infiltration rate at the ground surface is taken as the upper boundary condition, and the lower boundary condition is assumed to be a zero-flux condition at the interface between the soil layer and the bedrock. Evapotranspiration and sublimation are estimated using the maximum entropy production-based model proposed by Wang et al. (2009). In a previous study, GBEHM-RS was developed and successfully applied to simulate frozen soil in the upper Yellow River Basin (Zheng et al., 2019). In the current study, GBEHM-RS is applied to the entire TP, with a much larger spatial extent and more complex climate, topography, and landscape conditions.

3.2. Model setup

The study region was divided into 1 × 1 km grid-cells. In each grid, the modelling domain is from the soil (or snow, when existed) surface to 70 m below the surface. The underground region was divided into 149 horizontal layers with the thickness of each layer gradually increasing from 0.01 m near the ground surface to 4.0 m at the bottom. The model was run at a daily time step and the entire simulation period was from September 2002 to August 2016. To obtain the initial T_{soil}, liquid soil moisture, and soil ice content profiles, the ground measured T_{soil} profiles available at the 41 boreholes (varying from 20 m to 70 m deep) were firstly interpolated/extrapolated into the entire study region by applying a multilinear regression assisted with elevation and the multiyear-mean MODIS LST (Supplementary Text S1). It should be noted that except for the four GTN-P boreholes, the other 37 boreholes only provided one-time measurements of T_{soil} profiles and hence were not further used in model evaluation. The geothermal flux at the lower boundary was then estimated based on the temperature gradient near the domain bottom for each grid cell. The obtained spatially continuous T_{soil} profiles and lower boundary geothermal flux were applied in a model spin-up for 20 years (repeatedly driven by the climatic forcing

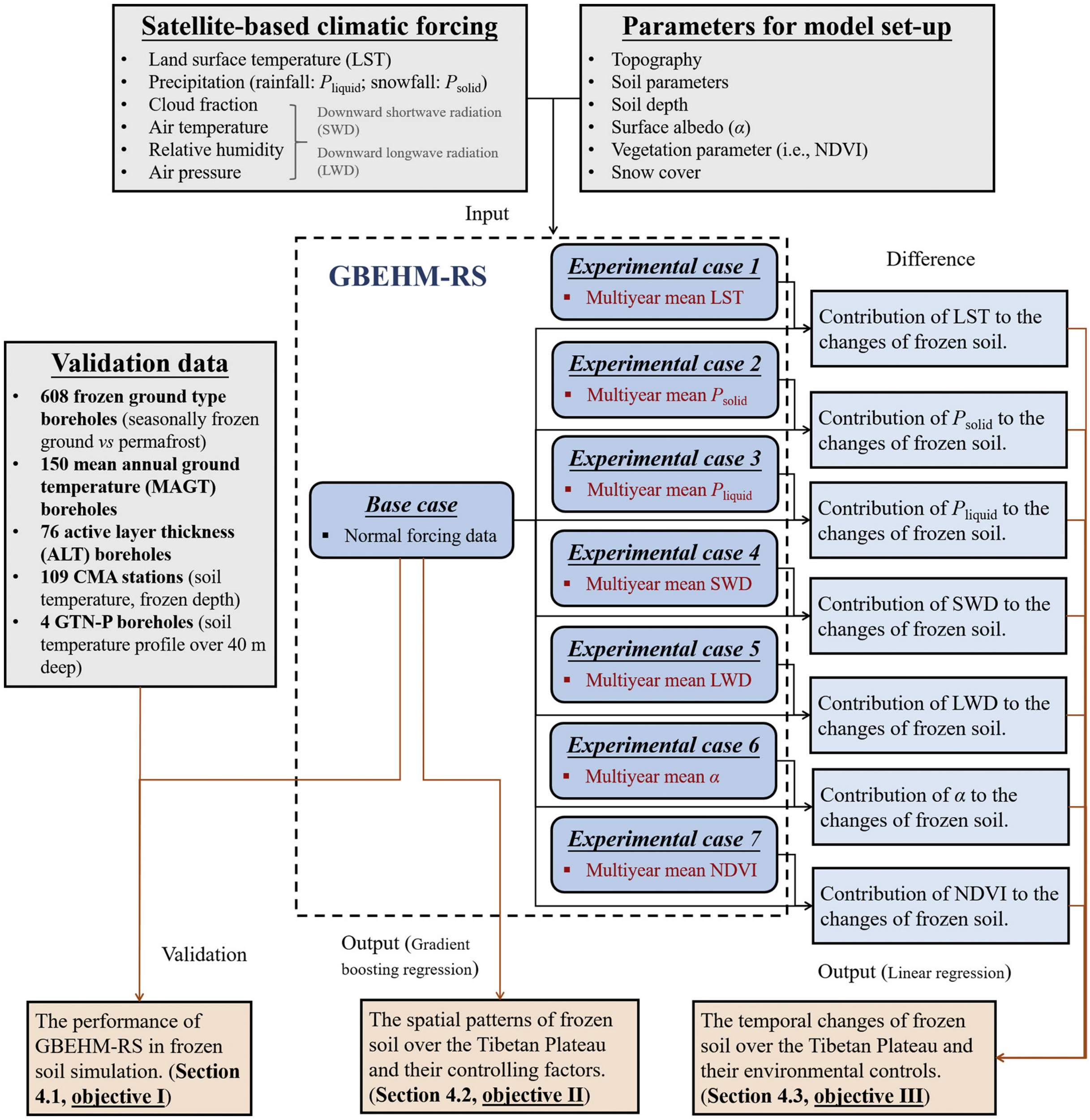

Fig. 2. Flow chart of the study. The boxes with grey background list all the external data. The boxes with blue background are modelling experiments. The boxes with red background are results. (For interpretation of the references to colour in this figure legend, the reader is referred to the web version of this article.)

during September 1st, 2002 – August 31st, 2003), and the initial conditions of T_{soil}, liquid soil moisture, and soil ice content were resultants of the model spin-up.

3.3. Experimental design

Eight independent simulation experiments (i.e., the *Base case* and *Experimental cases 1–7*) were carried out to evaluate the performance of GBEHM-RS in frozen soil simulation (objective I), to examine the simulated spatial patterns of frozen soil and their controlling factors (objective II), and to quantify the temporal changes of frozen soil and to identify their environmental controls (objective III) over the TP (see Fig. 2). The *Base case* uses the satellite-based climatic forcing and provides simulations of spatial patterns and temporal changes of frozen soil. Then, the model performance is assessed by validating the simulated frozen-ground types, MAGT, ALT, T_{soil}, and D_f against ground measurements. In addition, we also performed an uncertainty analysis on the satellite-based model inputs (i.e., LST, precipitation, SWD, LWD, and α) by adding a variation range to each input variable and assessing the model sensitivities to the input variations (see discussion and Supplementary Text S2). The spatial patterns of seasonally frozen ground and permafrost are represented by the annual maximum soil freeze depth (SFD) and the annual maximum active layer thickness (ALT), respectively. The relative importance of relevant factors (i.e., LST, P_{solid}, P_{liquid}, SWD, LWD, topography, vegetation, and soil parameters) in shaping the spatial patterns of SFD and ALT are quantified using the gradient boosting regression approach, which is consisted of a sequence of models and is suitable for assessing the relations between a predictive variable and driving factors (Breiman, 2001; Karjalainen et al., 2019) (also see Supplementary Text 3).

In the *Experimental cases 1–7*, the temporal changes of LST, P_{solid}, P_{liquid}, LWD, SWD, α, and NDVI are respectively neglected by using the multiyear mean forcing data from 2002 to 2016 for each year. The differences between the *Experimental cases 1–7* and the *Base case* (referred to as D_x, x = LST, P_{liquid}, P_{solid}, SWD, LWD, α, and NDVI) respectively represent the influences of variable x on the temporal changes of frozen soil (Mao et al., 2015). Then, the model simulated changes of frozen soil (D) are estimated using a linear combination of these seven individual differences (Eq. [1]). The relative contribution of x to the temporal changes of frozen soil (C_x) is quantified as the ratio of the covariance of D and D_x over the variance of D (Eq. [2]; Zhou et al., 2017).

$$D \approx \sum_x \beta_x \cdot D_x + \beta_0 \tag{1}$$

$$C_x = \frac{Cov(\beta_x \cdot D_x, D)}{Cov(D, D)} \tag{2}$$

where β_x and β_0 are fitting coefficients.

4. Results

4.1. Validation of satellite-based simulation of frozen soil

4.1.1. Spatial distributions of seasonally frozen ground and permafrost

In this study, permafrost is defined as the area with T_{soil} at any depth between 0 and 70 m deep remaining at or below the freezing point (0 °C) for at least two consecutive years, otherwise, the ground is identified as seasonally frozen ground (with annually freezing and thawing) or unfrozen ground (with T_{soil} remaining positive for the entire period) (van Everdigen, 1998). Fig. 3 depicts the mean spatial distribution of permafrost and seasonally frozen ground during 2002–2016, with each specific frozen ground type remained longer than half of the entire simulation period. Compared with the field observations at the 608 boreholes, the model has obtained a high accuracy with 86.3% (158/183) of seasonally frozen ground boreholes and 79.1% (336/425) of permafrost boreholes being accurately identified. For the boreholes that are not accurately identified by the model, they are almost entirely located near (within a typical distance of ~2 km) the boundaries between the permafrost and seasonally frozen ground. In these transition zones, the landscape usually exhibits higher spatial heterogeneities and changes in frozen ground types mainly occur, which lead to greater difficulties in the accurate determination of frozen ground types in these regions (Cao et al., 2019; Obu et al., 2019).

Table 2
Coefficient of determination (R^2), mean bias, and root-mean-squared error (RMSE) for simulated daily mean soil temperature (T_{soil}) and 7-day-mean frozen depth (D_f) against ground measurements at CMA stations.

	Depth (m)	R^2	Mean bias (°C)	RMSE (°C)
Daily mean T_{soil}	0.05	0.88	−0.27	3.25
	0.1	0.90	−0.33	2.89
	0.15	0.91	−0.35	2.66
	0.2	0.91	−0.32	2.50
	0.4	0.91	−0.28	2.35
	0.8	0.90	−0.36	2.11
	1.6	0.88	−0.33	1.81
	3.2	0.84	−0.30	1.61
	All the depths	0.90	−0.32	2.53
	Elevation range (m)	R^2	Mean bias (m)	RMSE (m)
7-day-mean D_f	2000–2500	0.43	0.00	0.28
	2500–3000	0.57	+0.02	0.31
	3000–3500	0.58	+0.02	0.35
	3500–4000	0.75	+0.03	0.26
	4000–5000	0.67	+0.05	0.42
	All the ranges	0.65	+0.04	0.35

4.1.2. T_{soil} and D_f over seasonally frozen ground

Statistical results of the comparison between observed and simulated T_{soil} at eight observational depths (i.e., 0.05, 0.1, 0.15, 0.2, 0.4, 0.8, 1.6, and 3.2 m) at the 109 CMA stations are summarized in Table 2. Note that all the CMA stations are located on the seasonally frozen ground. Results show that GBEHM-RS performed very well in reproducing observed T_{soil} at all depths, with the coefficient of determination (R^2; calculated using the Eq. [A3] in Appendix A) ranging from 0.84 to 0.91, RMSE ranging from 1.61 °C to 3.25 °C, and mean bias ranging from −0.36 °C to −0.27 °C. In addition to the overall accuracy, GBEHM-RS also performs reasonably well in capturing the temporal changes of T_{soil} at each depth (Supplementary Fig. S7).

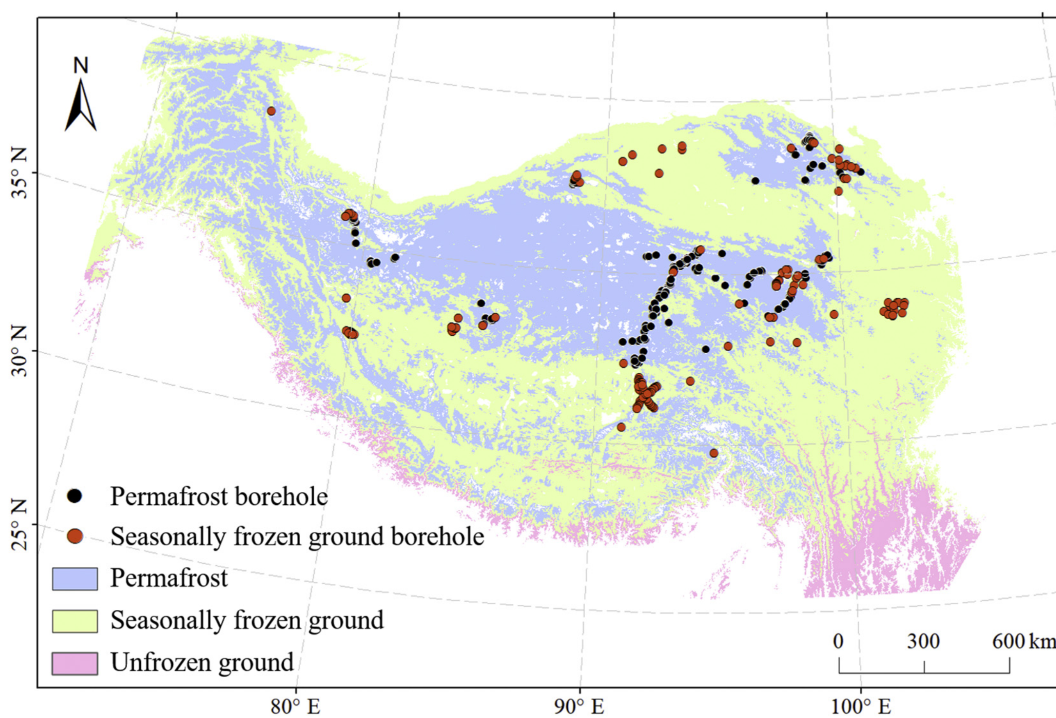

Fig. 3. Spatial patterns of simulated permafrost, seasonally frozen ground, and unfrozen ground in the Tibetan Plateau. The ground-measured frozen ground types at 608 boreholes are also shown for comparison.

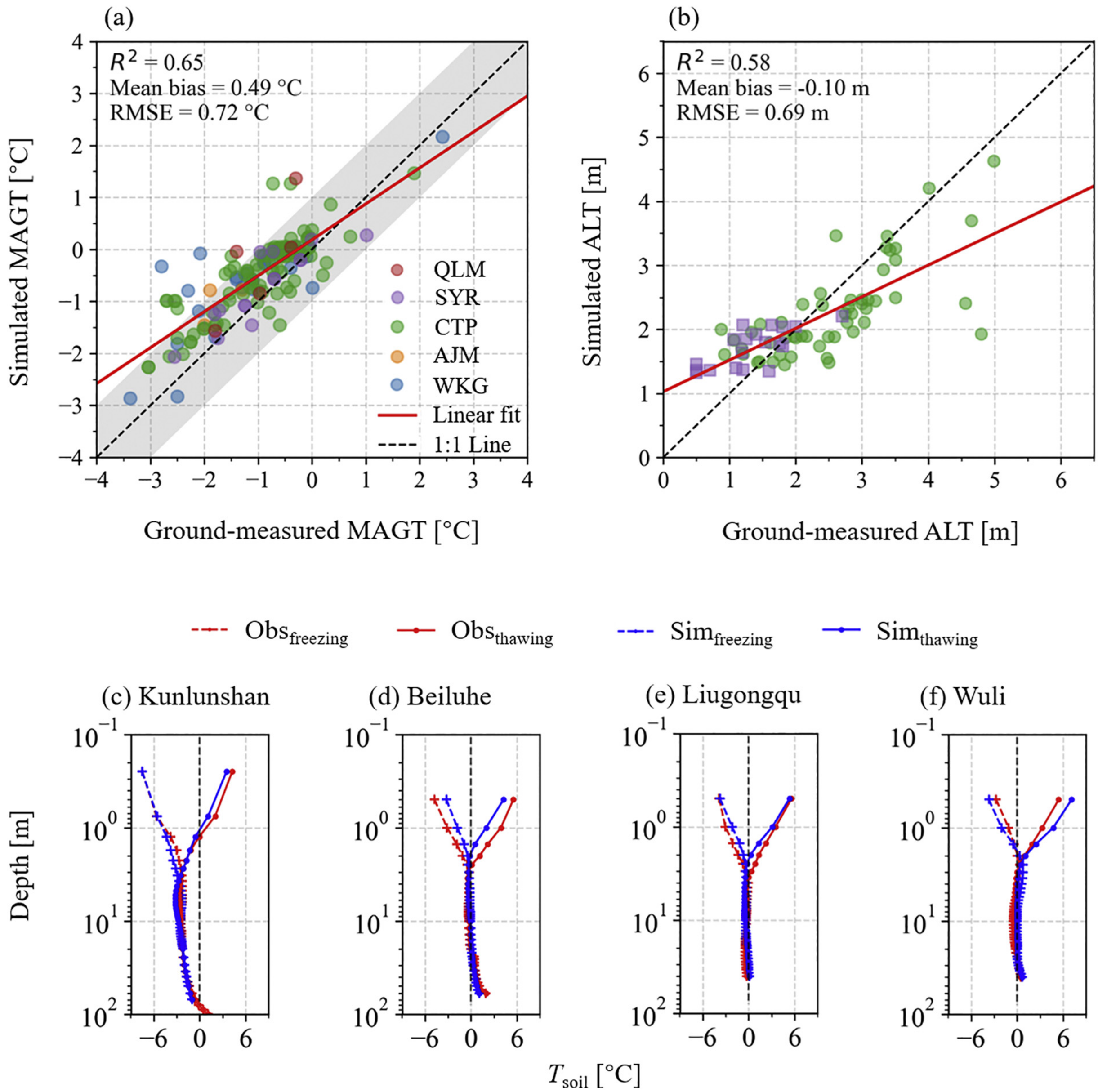

Fig. 4. Comparison of the simulated (Sim) and observed (Obs) mean annual ground temperature (MAGT), active layer thickness (ALT), and deep-ground soil temperature (T_{soil}) profiles at permafrost boreholes. In parts (a) and (b), all the permafrost boreholes are divided into five groups based on their locations, i.e., the Qilian Mountains (QLM, red), the source region of Yellow River (SYR, magenta), the central Tibetan Plateau (CTP, green), the Aerjin Mountains (AJM, yellow), and the west Kunlun and Gaize (WKG, blue). The shaded region indicates that the differences between simulated and observed MAGT are within ± 1 °C. The black dashed lines are 1:1 lines and the red lines show the best linear fit. Parts (c)–(f) show the deep-ground T_{soil} profiles during the freezing (from October to next April, dashed line) and thawing (May–September, solid line) seasons at Kunlunshan, Beiluhe, Liugongqu, and Wuli, respectively; note that a logarithmic scale is used for the y-axis. (For interpretation of the references to colour in this figure legend, the reader is referred to the web version of this article.)

Due to small changes between adjacent days, the assessment of simulated D_f is performed on a 7-day-mean basis. Overall, the satellite-based simulation well reproduces the observed D_f, resulting in an R^2 of 0.65, RMSE of 0.35 m, and mean bias of +0.04 m (Table 2). To gain further insights into the model performance in different regions, we split the CMA stations into five groups along an elevation range, i.e., 2000–2500, 2500–3000, 3500–4000, 4000–4500, and 4000–5000 m a.s.l. (Table 2). In general, the simulated D_f agrees reasonably well with ground measurements for each elevation range, despite relatively larger discrepancies when the measured D_f is shallow (e.g., less than 0.1 m), which can be mainly caused by a small mismatch in the ending dates of soil freezing and thawing between simulation and observation (Supplementary Fig. S8). The validity of the model in simulating both long-term trend and inter-annual variability of D_f across elevation ranges is further confirmed by a close agreement between observed and simulated SFD anomalies (Supplementary Fig. S9).

4.1.3. MAGT, ALT, and deep-ground T_{soil} at permafrost

The comparison of measured and simulated MAGT at 150 permafrost boreholes is shown in Fig. 4a. Despite a slight warming bias (+0.49 °C), the simulated MAGT were generally close to these ground measurements (R^2 of 0.65 and RMSE of 0.72 °C) and the simulated errors at 88% (133 out of 150) boreholes were within ± 1 °C. To further evaluate the model performance in simulating the spatial patterns of permafrost thermal status, we divided all the boreholes into five groups based on their locations, i.e., the Qilian Mountains (QLM), the source region of Yellow River (SYR), the central Tibetan Plateau (CTP), the Aerjin Mountains (AJM), and the west Kunlun and Gaize (WKG) (Figs.

S4a and 4a). Within each region, the simulated and observed MAGT are also close to each other with the mean biases ranging between +0.20 °C and + 0.77 °C. Fig. 4b shows the comparison of simulated and observed ALT at 76 permafrost boreholes. Again, our simulated ALT also reasonably follows observation, with an R^2 of 0.58, mean bias of −0.1 m, and RMSE of 0.69 m. These validation results indicate that GBEHM-RS can capture the spatial patterns of permafrost thermal status in the TP with reasonable accuracy.

At the four GTN-P boreholes (i.e., Kunlunshan, Beiluhe, Liugongqu, and Wuli; Fig. 1), Fig. 4c-f compared the simulated and ground-measured T_{soil} profiles during the freezing (i.e., from October to next April) and thawing (i.e., from May to September) seasons. Compared with in situ observations, the satellite-based model performs generally well in reproducing the variations of T_{soil} along depth with a typical accuracy of ± 1.0 °C, despite relatively larger biases for near-surface T_{soil} at the Beiluhe and Wuli sites (Fig. 4d and f). For near-surface soil, the modelled T_{soil} represents a combination of T_{soil} for all landscape covers (e.g., water bodies, snow, and vegetation) within the 1 × 1 km domain, which might differ markedly from the site-level observations. However, this scale mismatch-induced difference gradually diminishes as the depth increases. Finally, we used the ground-measured near-surface (~0.5 m) and deep-ground (~10 m) T_{soil} at four GTN-P boreholes to validate the model performance in simulating the temporal changes of T_{soil} in permafrost (see supplementary Fig. S10). Results show that the simulated and measured T_{soil} dynamics are generally close at both depths, indicating a reasonable performance of GBEHM-RS in reproducing the dynamic evolutions of ground thermal regimes of permafrost in the TP.

4.2. Spatial distribution of frozen soil and climatic controls over the TP

4.2.1. Spatial patterns of frozen ground types, liquid soil moisture, and soil ice content

The multiyear-mean spatial pattern of simulated frozen ground types (i.e., the permafrost, seasonally frozen ground, and unfrozen ground) during 2002–2016 is illustrated in Fig. 3. The seasonally frozen ground covers a total area of 1.83 million km^2 (or ~ 56%) and mainly occupies the lower plains and river valleys in the southern and eastern TP. The permafrost covers an area of 1.22 million km^2 (or ~ 37%) and is primarily distributed over mountain ranges in the northern and western plateau. The unfrozen ground covers an additional area of 0.22 million km^2 (or ~ 7%) and is mainly located on the southern and southeast edges of the plateau. Fig. 5 shows the distribution of permafrost fraction (f_P, and the fraction of seasonally frozen ground is 100% minus f_P) as a function of elevation, LST and P_{solid}. It is found that permafrost generally starts to occur at an elevation of ~3600 m a.s.l, above which, the f_P steadily increases at a rate of ~4.4% per 100 m (Fig. 5a). In comparison, the f_P is much more sensitive to changes in LST around the freezing point. With the increase of mean annual LST from −0.57 °C to +1.04 °C, the f_P decreases sharply from 90% to 10% (Fig. 5b). For f_P of 50%, it corresponds to a mean annual LST of +0.42 °C, which is close to the threshold (i.e., +0.5 °C) used by Wang et al. (2006) to delineate the lower limit of permafrost. Additionally, f_P increases with the increase of P_{solid} (Fig. 5c), especially for regions with a mean annual P_{solid} less than ~25 mm yr^{-1}. For regions with a mean annual P_{solid} higher than ~25 mm yr^{-1}, the f_P only slowly increases with the increase of P_{solid}.

In addition to frozen ground types, we also examine the spatial patterns of annual mean liquid soil moisture and soil ice content for the top 5 m soil layer, where the soil freezing/thawing processes mainly occur (Supplementary Fig. S11). Similar to the spatial pattern of P_{liquid} (Supplementary Fig. S1), the liquid soil moisture is relatively higher in the southeast region (> 1.2 × 10^3 kg m^{-2}) and gradually decreases towards northwest with the lowest liquid soil moisture found in the Qiangtang Plateau (0.3–0.6 × 10^3 kg m^{-2}; Supplementary Fig. S2). In comparison, soil ice exists in regions with a relatively lower LST and the spatial pattern of soil ice content is similar to that of the thawing index (Supplementary Fig. S1), with the annual mean soil ice content within 0–5 m soil column relatively higher in permafrost regions (> 400 kg m^{-2}) and relatively lower (< 50 kg m^{-2}) in seasonally frozen ground.

4.2.2. Spatial pattern of mean annual SFD for seasonally frozen ground

Fig. 6a illustrates the spatial pattern of simulated mean annual SFD over the entire TP during 2002–2016. The simulated SFD varies between 0.03 m and 5.94 m over the TP and has a mean value of 1.29 m. The magnitude of SFD shows a strong elevation dependence (Fig. 6b). Smaller SFDs are obtained along the southern edge of the TP where elevation is generally lower than 3000 m a.s.l, whereas larger SFDs primarily locate near the lower limit of permafrost in the central and northeast plateau with an elevation typically above ~4500 m a.s.l. To examine the controlling factors of the SFD spatial pattern, we investigated the relative importance of relevant factors (i.e., LST, P_{solid}, P_{liquid}, SWD, LWD, α, topography, vegetation, and soil parameters) in shaping the spatial pattern of SFD. We find that the spatial pattern of SFD is mainly controlled by four climatic factors, i.e., freezing index (the cumulative negative daily mean LST within a year), thawing index (the cumulative positive daily mean LST within a year), P_{solid}, and P_{liquid}, whereas other factors only exert minor effects (Supplementary Fig. S6). Fig. 6c illustrates the relative importance of these four climatic factors in shaping the SFD spatial pattern along an elevation gradient. It is found that temperature, in particular the freezing index, dominantly controls the spatial pattern of SFD at all elevation ranges. However, as elevation increases, the relative importance of freezing index steadily decreases, while the relative importance of other factors increases. This is especially evident for the thawing index, which suggests an increased impact of LST during the antecedent thawing season on SFD spatial variations in higher elevated regions.

4.2.3. Spatial pattern of mean annual ALT over permafrost

The multiyear-mean spatial pattern of simulated ALT over permafrost during 2002–2016 is shown in Fig. 6d. Over the study region, the simulated ALT varies between 0.05 m and 10.24 m with an average ALT of 1.85 m. Similar with SFD, ALT also exhibits a clear elevation dependence, with smaller ALTs distributing in the hinterland of the Qiangtang Plateau and high-rising mountain tops and larger ALTs occurring in areas near the water bodies and the lower limit of permafrost, such as the source regions of the Yellow, Yangtze, and Nu Rivers (Fig. 6d and e). In addition, the same four climatic factors (i.e., the freezing index, the thawing index, P_{liquid}, and P_{solid}) are also found to primarily control the spatial pattern of ALT (Supplementary Fig. S6). Among them, the thawing index shows the highest importance in shaping the spatial distribution of ALT and its importance also generally increases with elevation (Fig. 6f). In comparison, the other three climatic factors are relatively less important, except for the freezing index in relatively low-elevation regions.

4.3. Temporal changes of frozen soil and the climatic controls

4.3.1. Temporal changes of frozen ground types, liquid soil moisture, and soil ice content

The changes in spatial coverages of permafrost and seasonally frozen ground are assessed by comparing the mean annual distributions of permafrost and seasonally frozen ground in two sub-periods during 2002–2016, i.e. the first (2002–2007) and last (2011–2016) six years. This treatment reduces simulation uncertainty at short temporal scales and provides a more reliable assessment of long-term changes. Compared with 2002–2007, over the entire plateau area, permafrost disappears in ~7.5 × 10^4 km^2 (6.0%) regions in the early 2010s. Evident permafrost degradations are found in the southeast plateau, covering the source regions of several large rivers, i.e., the Yangtze, Yellow, Nu, Lancang, and Brahmaputra Rivers (Fig. 7a). In comparison,

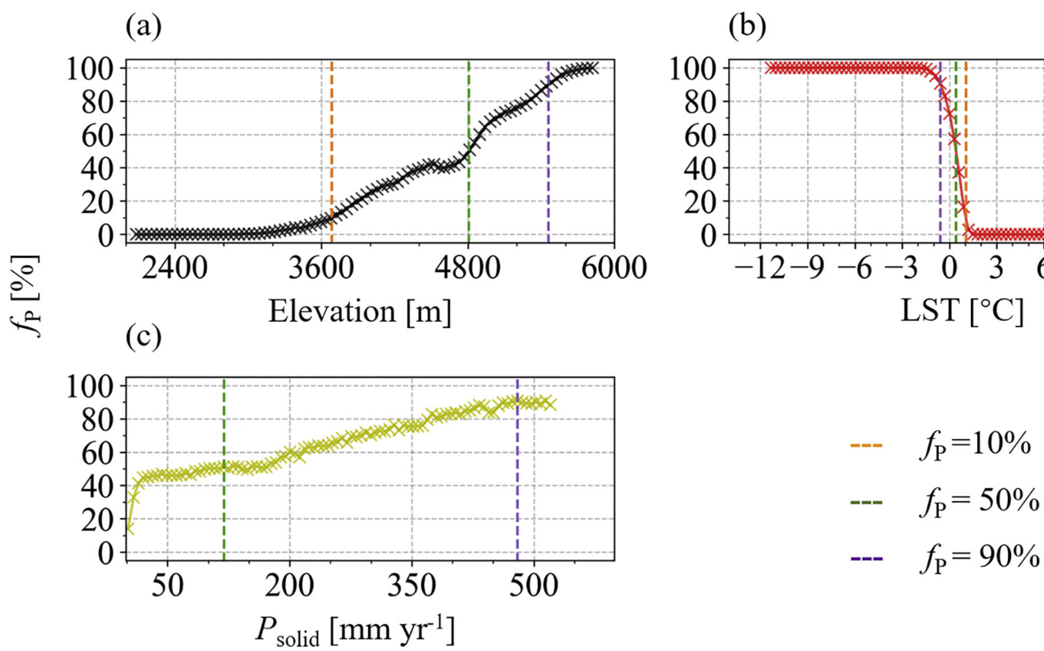

Fig. 5. Changes of permafrost fraction (f_p) with elevation, land surface temperature (LST), and snowfall (P_{solid}). Locations with f_p of 10%, 50%, and 90% are indicated by the orange, green and purple lines, respectively. (For interpretation of the references to colour in this figure legend, the reader is referred to the web version of this article.)

newly formed permafrost is only presented in ~1.3 × 10^4 km^2 (1.1%), which primarily occurs in the regions between the Yellow and Yangtze Rivers and around the Karakoram and Gangdise Mountains (Fig. 7a). With the rapid degradation of permafrost, the soil ice content also experienced a notable decline during the study period (i.e., at a rate of ~ -15 kg m^{-2} yr^{-1} in the source regions of Yellow and Yangtze Rivers; Supplementary Fig. S11d). The melted ice provides additional water supply and leads to increased liquid soil moisture (Supplementary Fig. S11c). In addition to soil thawing, the increase of P_{liquid} also contributes to the increase of liquid soil moisture, such as in the Brahmaputra River Basin in the south of the TP (see Fig. 1 and Supplementary Figs. S11c vs S12c).

4.3.2. *Temporal changes of SFD for seasonally frozen ground*

The spatial pattern of the SFD trend during 2002–2016 is shown in Fig. 7b. Note that the SFD trend is only calculated for regions with a persistent seasonally frozen ground over the study period (Fig. 7a). During the simulation period, the SFD trend varies between -8.92 cm yr^{-1} and $+3.77$ cm yr^{-1} with a mean value of -0.50 cm yr^{-1}, indicating an overall small decrease of SFD. Larger decreases in SFD mainly exist in high elevation regions (> 3800 m a.s.l.), such as the northern edge of the TP, the regions between the Tanggula and Nyainqentanglha Mountains, and the Hengduan Mountains. In contrast, the increases of SFD are most evident in lower elevation regions, including the southern and western edges of the TP, the Qaidam Basin, and the northeast TP (Figs. 1 and 7b, and Supplementary Fig. S2). The spatial pattern of the SFD trend is very similar to that of the freezing index trend (Supplementary Fig. S12a), suggesting a predominant role of LST in controlling the changes of seasonally frozen soil. However, except for a few scattered areas (~9%) adjacent to the lower limit of permafrost, the SFD trends in other places are statistically non-significant ($p \geq .05$; see Supplementary Fig. S13a). To further confirm the role of LST on SFD changes, we explore the relationship between changes in SFD and freezing index and find significant ($p < .05$) correlations over most of the seasonally frozen ground (~66%). Nonetheless, non-significant ($p \geq .5$) correlations between SFD and freezing index are found primarily in regions near the lower limit of permafrost (e.g., the circled regions *1–4* in Fig. 8a), where the changes of SFD tend to show significant correlations with changes of annually accumulated snow depth and annual mean soil water content (the sum of soil water in both liquid and soil phases within 0–5 m soil column) (Fig. 8b and c), indicating important roles of snow cover and soil water in the control of SFD temporal changes in these regions.

We then compared the estimated SFD changes from the *Base case* respectively with those from *Experimental cases 1–7* to quantify the relative contribution of each driving factor (Fig. 9). Results show that nearly all of the temporal changes of SFD are controlled by three climatic factors (i.e., LST, P_{solid}, and P_{liquid}; Fig. 9a), among which, LST dominates SFD changes in ~80% of the seasonally frozen ground. This is most evident in low-elevation areas, such as the Qaidam Basin and the southeast TP (Fig. 9a, b and e). As elevation increases, the contribution of LST gradually decreases, from over 80% in the low-elevation areas (2000–2200 m a.s.l) to less than 50% in the high-elevation regions (> 4800 m a.s.l). In comparison, regions where the changes in SFD dominantly controlled by P_{solid} and P_{liquid} are much fewer. The P_{solid}-controlled areas occupy ~12% of the seasonally frozen ground (Fig. 9c and e) and are mainly located in the Qilian Mountains, the source regions of the Yellow, Yangtze, and Nu Rivers, and the conjectures of Karakoram and Kunlun Mountains. These regions also correspond to places with significant correlations between annually accumulated snow depth and SFD (the circled regions *1–4* in Fig. 8). This implies that P_{solid} exerts impact on the changes of seasonally frozen ground mainly through its impact on snow cover changes. In comparison, the P_{liquid}-controlled areas cover ~6% of the seasonally frozen ground, including the Nyainqentanglha Mountains, the Gangdise Mountains, the Tanggula Mountains, and the regions around the Qaidam Basin with a typical arid climate (Fig. 9d and e). Over these regions, the temporal changes of soil water content generally show significant ($p < .05$) correlations with those of SFD, implying that the impact of P_{liquid} on frozen soil is primarily through its impact on soil water content. Moreover, different from the contribution of LST that decreases with elevation, the contributions of P_{solid} and P_{liquid} gradually increase as the elevation increases, from ~6% and ~ 3% below 2200 m a.s.l to both higher than 13% above 4600 m a.s.l, respectively (Fig. 9a, c, and d). Compared with the above three climatic factors, regions

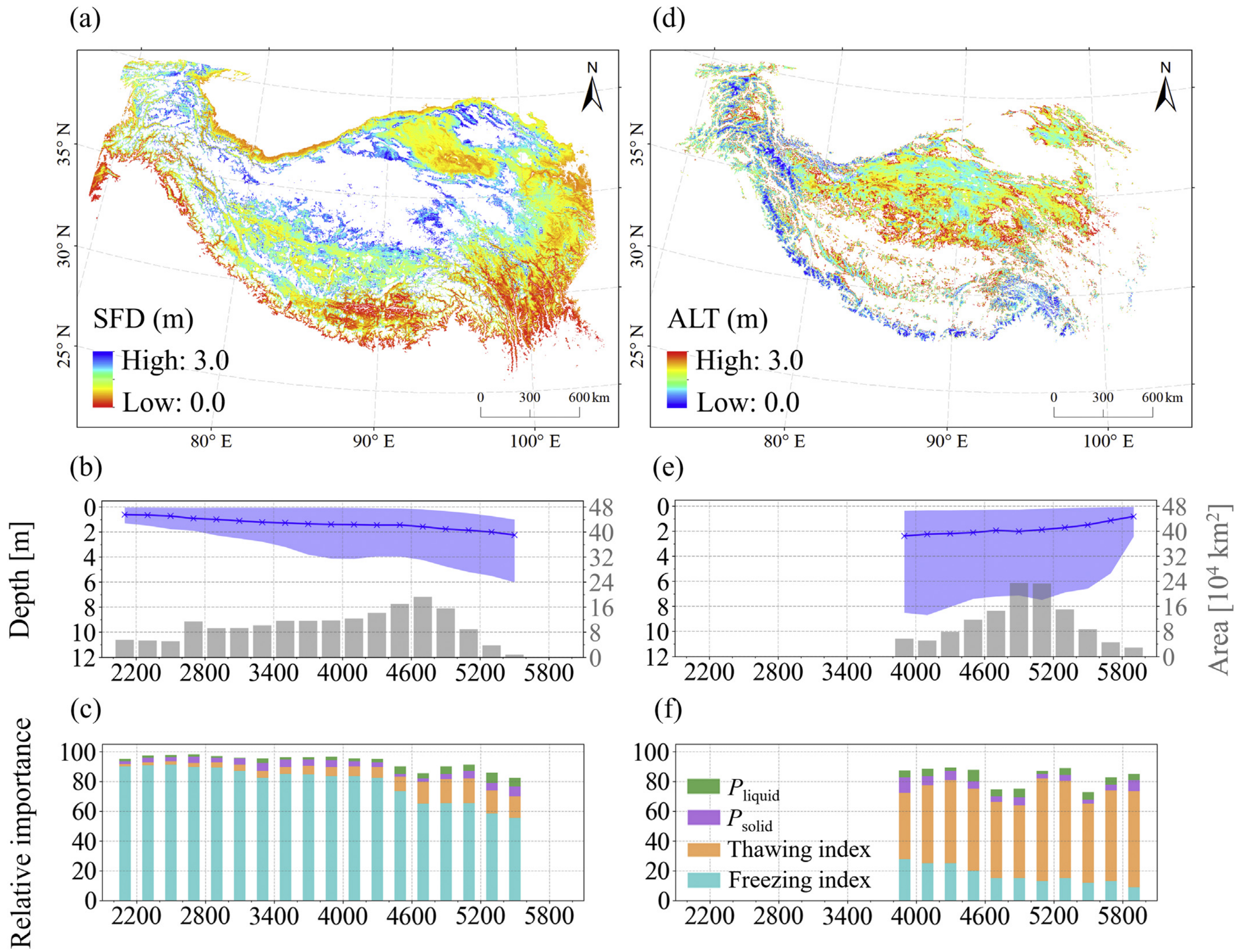

Fig. 6. The mean annual spatial patterns of annual (a) maximum soil freeze depth (SFD) and (d) maximum active layer thickness (ALT) during 2002–2016. Part (b) shows the distributions of SFD (blue) and seasonally frozen ground area (grey) along an elevation gradient; the solid line indicates the mean value and the shaded area is the spread of SFD within each elevation zone. Part (e) shows the distributions of ALT (blue) and permafrost area (grey) along an elevation gradient; the solid line indicates the mean value and the shaded area is the spread of ALT within each elevation range. Parts (c) and (d) illustrate the relative importance of freezing index, thawing index, snowfall (P_{solid}), and rainfall (P_{liquid}) in shaping the spatial distributions of SFD and ALT along an elevation gradient, respectively. (For interpretation of the references to colour in this figure legend, the reader is referred to the web version of this article.)

where SFD changes are dominantly controlled by the other factors (i.e., SWD, LWD, α, and NDVI), are negligibly small and scattered (occupy ~2% of the seasonally frozen ground; see Supplementary Fig. S14).

4.3.3. Temporal changes of ALT over permafrost

The temporal changes of ALT during 2002–2016 and the controlling factors are also only examined in regions where permafrost is persistent throughout the entire study period. Different from that of SFD, ALT has been mainly increasing over the permafrost regions during the study period. Over the entire plateau, the ALT trend varies between -34.60 cm yr^{-1} and $+46.99$ cm yr^{-1}, with an average trend of $+3.17$ cm yr^{-1} (Fig. 7c). Additionally, the ALT trends are statistically significant ($p < .05$) in over 25% of the permafrost areas (Supplementary Fig. S13b), including the source regions of the Yellow and the Yangtze Rivers, the southern Qiangtang Plateau, and the Nyainqentanglha Mountains (Figs. 1 and 7c, and Supplementary Fig. S2). These results suggest an overall rapid degradation of TP permafrost during the study period.

The spatial pattern of ALT trends is similar to that of thawing index trends (Fig. 7c vs Fig. S12b), with a significant ALT-thawing index relationship ($p < .05$) found in ~73% of the permafrost regions, implying a predominant role of LST in controlling permafrost changes. However, non-significant ($p \geq .05$) correlations between ALT and thawing index are also evident and are mainly distributed in the source regions of the Yellow and Yangtze Rivers (see circled region 2 in Fig. 10a) and the Karakoram Mountains (Supplementary Fig. S2). In these regions, the correlation between the ALT and annually accumulated snow depth and/or annual mean soil water content becomes significant ($p < .05$; Fig. 10b and c), implying the potential impacts of P_{liquid} and P_{solid} on permafrost changes.

The contributions of LST, P_{liquid}, P_{solid}, and other factors (i.e., SWD, LWD, α, and NDVI) to the temporal changes of ALT are again, quantified by comparing the *Base case* and *Experimental cases 1–7*. Similar to SFD, the temporal changes of ALT are also primarily controlled by the three climatic factors (i.e., LST, P_{solid}, and P_{liquid}). Among them, LST plays a dominant role in controlling the ALT changes in ~80% of the permafrost region, and the contribution of LST shows a general increasing trend with the increase of elevation (Fig. 11a, b, and e). In high-elevation regions, such as the western Qiangtang Plateau, the contribution of LST to the temporal changes of ALT can be greater than

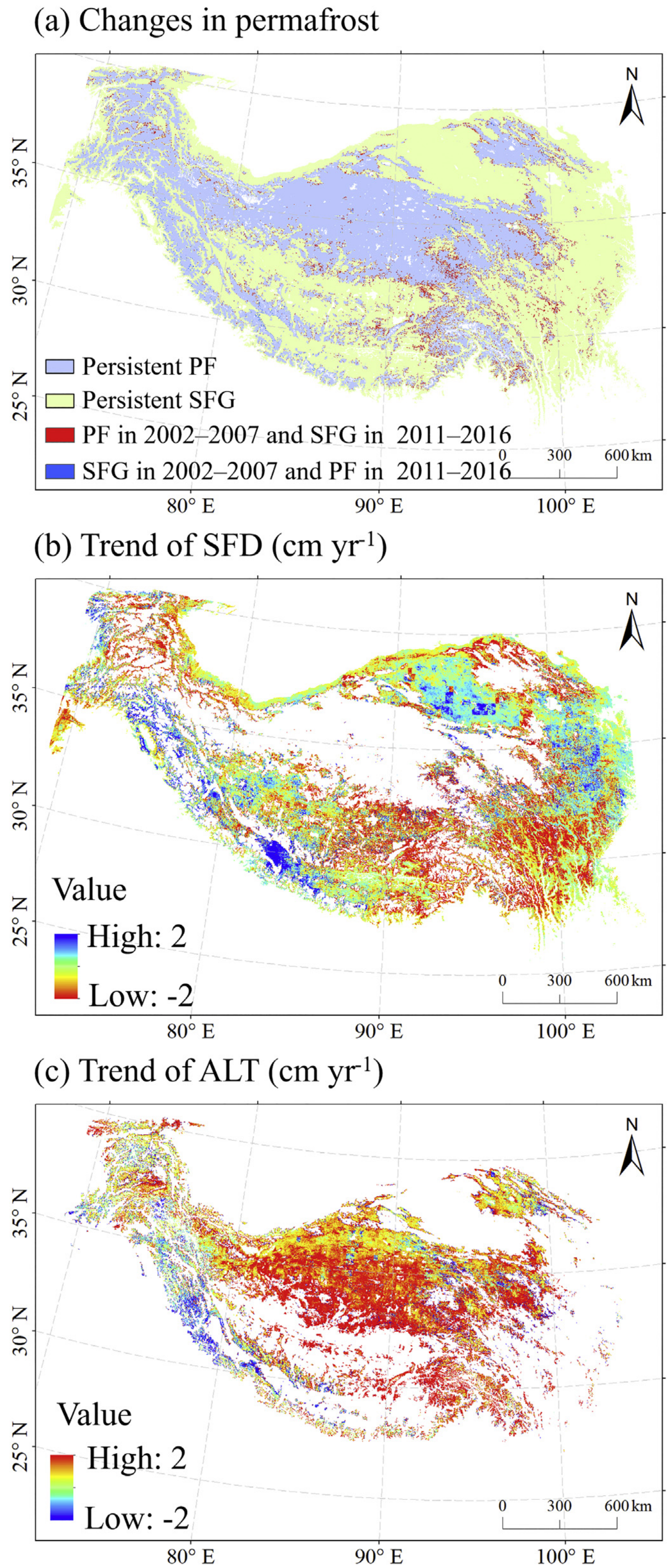

Fig. 7. Changes of the permafrost and seasonally frozen ground areas as well as the trends of the annual maximum soil freeze depth (SFD) and the annual maximum active layer thickness (ALT) during 2002–2016. 'PF' and 'SFG' denote permafrost and seasonally frozen ground, respectively.

90% (Fig. 11b). As the elevation decreases, the permafrost area moves towards the source regions of Yellow and Yangtze Rivers, where the contribution of LST decreases and the contributions of P_{solid} and P_{liquid} increase. The P_{solid}-controlled and P_{liquid}-controlled areas account for ~11% and ~ 6% of the entire permafrost region, respectively (Fig. 11e). Moreover, the P_{solid} (P_{liquid}) -dominated regions roughly overlap with regions having significant correlations between snow depth (and soil water content) and ALT (Figs. 11c vs 10b, 11d vs 10c), which again indicates that the influences of P_{solid} (and P_{liquid}) on the permafrost changes are primarily through their influences on snow cover (and soil water content) changes. Additionally, the SWD, LWD, α, and NDVI-controlled areas are very limited (~3% of the permafrost regions) and their contributions to the temporal changes of ALT are also generally small (see Supplementary Fig. S15).

5. Discussion

The comprehensive validations against ground measurements of frozen ground types, MAGT, ALT, T_{soil}, and D_f approve the reliability of using process-based model driven by satellite data to reproduce the ground thermal regime of permafrost and seasonally frozen ground in the TP region (Figs. 3 and 4, and Supplementary Figs. S7–S10). Using GBEHM-RS, we quantified the spatiotemporal changes of frozen soil over the TP since the beginning of the 21st century. Overall, our simulated spatial patterns of frozen ground types, SFD, and ALT are consistent with previous studies (Cao et al., 2019; Pang et al., 2006; Peng et al., 2017; Wang et al., 2019a; Wu et al., 2018). To further evaluate the accuracy of simulated frozen soil, we collected seven frozen ground maps produced previously during 2002–2016 for the TP (Obu et al., 2019; Qin et al., 2017; Shi et al., 2018; Wang et al., 2006; Wang et al., 2019a; Wang et al., 2019b; Wu et al., 2018; Zou et al., 2017; Supplementary Table S2) and compared them with our estimates. Based on the validation of the various estimates against the frozen ground observations at 608 boreholes (see Table S2), we found the satellite-based maps were more likely to show higher and more consistent accuracy (~80%) in identifying both the permafrost boreholes and seasonally frozen ground boreholes, whereas the ground-based maps tended to exhibit a lower accuracy (~65%) in identifying the seasonally frozen ground boreholes. This finding is consistent with that of Zheng et al. (2019) in the head regions of the Yellow River, highlighting the potential advantage of satellite data in improving the spatial consistency of frozen soil simulations in the TP. Additionally, the satellite-based simulations of frozen soil over the TP have a much higher spatial resolution (~1 km) than those of ground-based ones (e.g., ~10 km in Qin et al. (2017) and Wu et al. (2018)). Since the TP is characterized as a mountainous frozen soil region with complex climate, topography, and landscape conditions, the satellite-based simulations with a higher spatial resolution are able to better capture the local spatial variabilities of ALT and SFD (Zhao and Li, 2015).

Consistent with previous findings in the TP and other frozen soil regions (e.g., the Northern China and high latitude Northern Hemisphere; Frauenfeld and Zhang, 2011; Park et al., 2013; Peng et al., 2017; Zhang et al., 2005), our results also demonstrate the predominant role of the freezing (thawing) index in controlling the large-scale spatial variability of SFD (ALT). However, as moving towards the transition zones between permafrost and seasonally frozen ground, the importance of thawing (freezing) index of the antecedent season in shaping the SFD (ALT) spatial pattern becomes increasingly evident (Fig. 6c and f), which has been commonly neglected in previous SFD and ALT estimations (e.g., Frauenfeld and Zhang, 2011; Wang et al., 2019a; Peng et al., 2018). In principle, the freezing and thawing indexes respectively represent the cooling and warming ability of the climate (Westermann et al., 2015). When the freezing (thawing) index is much larger than the thawing (freezing) index, the freezing (thawing) index would completely counteract the influences of antecedent thawing (freezing) index, causing the ground thermal condition in the permafrost (seasonally frozen ground) to evidently deviate from the freezing point before the subsequent thawing (freezing) season, i.e., the ground memory of historical heat in the near-surface region is completely erased (e.g., Zou et al., 2017). Such regions are almost entirely

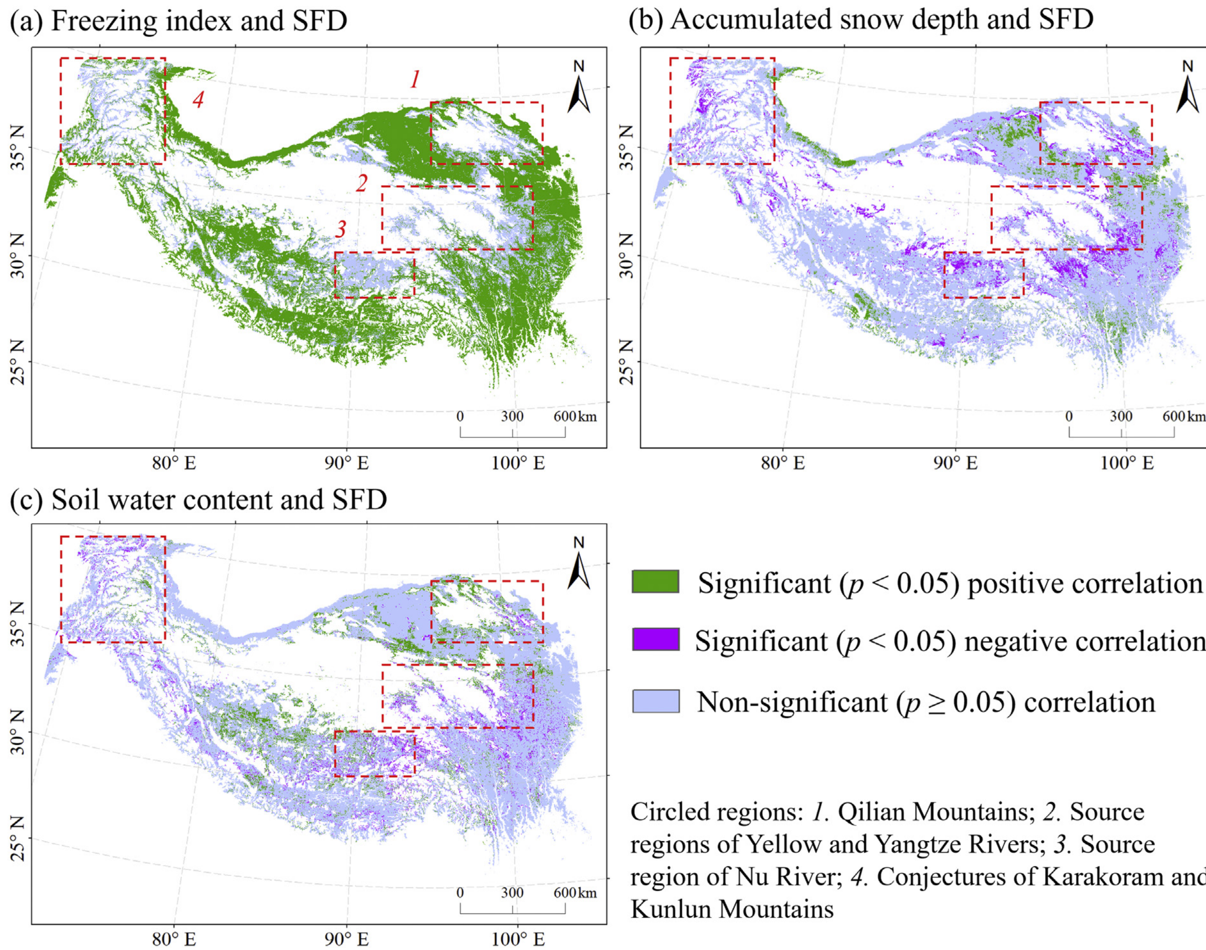

Fig. 8. Regions with significant ($p < .05$) and non-significant ($p \geq .05$) correlations between the changes of annual maximum soil freeze depth (SFD) and changes in (a) freezing index, (b) annually accumulated snow depth, and (c) annual mean soil water content (the sum of soil water in both liquid and soil phases within 0–5 m soil column) over seasonally frozen ground.

distributed far from the lower limit of permafrost (Supplementary Figs. S1b vs S1c). Within these areas, using freezing (thawing) index alone may obtain reliable SFD (ALT) estimates (Fig. 6c and f). Since the ground observations are usually located far from the lower limit of permafrost, it is thus not surprising that previous estimations of SFD and/or ALT without considering thermal conditions of the antecedent season are also generally satisfactory compared with ground observations (Peng et al., 2017; Wang et al., 2019a; Wu and Zhang, 2010). However, for regions near the lower limit of permafrost, the freezing and thawing indexes become equal and their net cooling (or warming) effects would accumulate, which may result in a much larger SFD or ALT (e.g., Ding et al., 2019). Without considering these two temperature indexes in the antecedent season would thus underestimate the magnitude and spatial variations of SFD (ALT) in regions near the lower limit of permafrost, which could partly explain the fact that our estimated SFD (ALT) varies much more rapidly than freezing (thawing) index (Figs. 6 vs S1) and is also much deeper (by ~1 m) than previous estimates over these areas (Ding et al., 2019; Pang et al., 2006; Peng et al., 2017; Wang et al., 2019a; Wu et al., 2010). In the TP, the places near the lower limit of permafrost overlap the source regions of many large rivers (Figs. 1 and 3) and are very sensitive to climate change (Zhang et al., 2004). Therefore, accounting for thermal conditions of the antecedent season so that to obtain a more accurate estimation of the frozen soil status in these areas is particularly important for understanding the interactions between the frozen soil, climate, ecosystem, and water cycles in the TP (Cheng and Wu, 2007; Jin et al., 2009; Zhao et al., 2019).

Regarding the temporal changes of frozen soil, we find that SFD shows both decreasing and increasing trends and the ALT exhibits an overwhelming increasing trend across the TP during 2002–2016. The rapid increases of ALT imply a notable degradation of permafrost on the TP, which is consistent with recent findings that temperature rising induced by the anthropogenic greenhouse gas emissions has been triggering the serious degradation of permafrost over the entire Northern Hemisphere (Biskaborn et al., 2019; Guo et al., 2020). Moreover, our study also found an evident asymmetric warming trends during the freezing and thawing seasons over the TP (i.e., a larger warming trend in summer than in winter; Supplementary Fig. S12). This is consistent with Guo et al. (2019) for 2001–2015 but different from other studies during earlier periods (e.g., before 2000) when winter experiences the largest warming trend among the four seasons (e.g., Wu et al., 2013). During recent decades, the seasonal warming pattern on the TP has been shifting from a dominant winter warming to a dominant summer warming, which is primarily caused by an enhanced snow-albedo feedback (Guo et al., 2019). Climate models project that the climate warming over the TP is going to continue towards the end of this century (Su et al., 2013), and if this asymmetric warming trend pertained or further intensified, a more pronounced summer warming is anticipated, which can result in a higher increasing rate of ALT and more serious permafrost degradation in the region.

In addition to temperature, we also highlight the contributions of P_{solid} and P_{liquid} to the temporal changes of frozen soils in the TP during 2002–2016. Our results suggest that P_{solid} exerts impacts on SFD through its impacts on snow cover (Figs. 8b and 9c). Due to the low

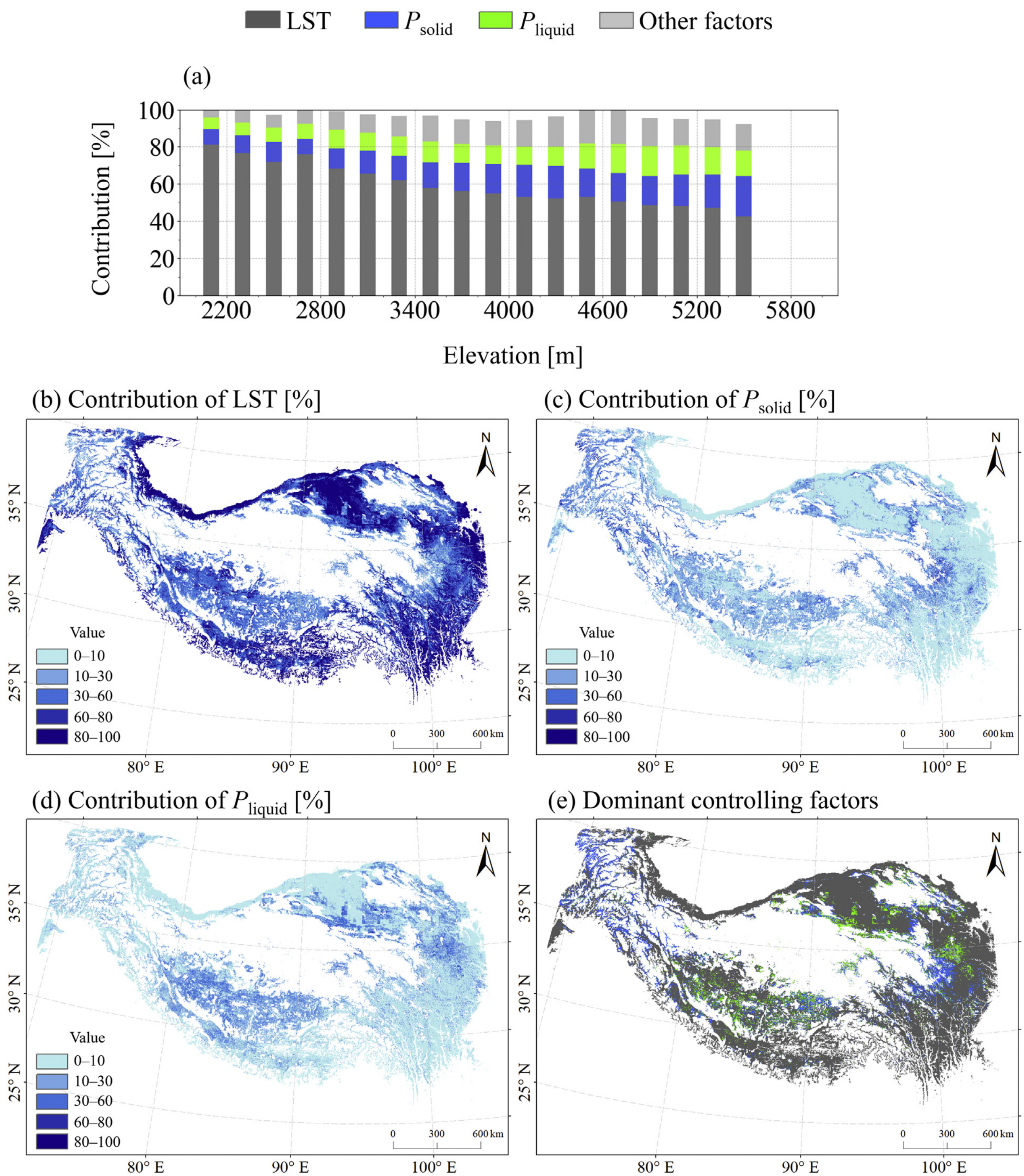

Fig. 9. Relative contributions of LST, P_{solid}, P_{liquid}, and other factors (sum of SWD, LWD, α, and NDVI) to the temporal changes of annual maximum soil freeze depth (SFD). Part (a) shows the relative contributions of LST, P_{liquid}, P_{solid}, and other factors along the elevation gradient. Parts (b)–(d) show the spatial patterns of the relative contributions by LST, P_{solid}, and P_{liquid}, respectively. Part (e) shows the locations of dominant controlling factors.

thermal conductivity (~0.2 W K^{-1} m^{-1}), the snow cover is a typical strong thermal insulator that would prohibit the exchange of heat between the atmosphere and the soil surface (Hardy et al., 2001; Zhang, 2005). Moreover, the snow insulation effects have both warming and cooling effects, depending on the phenology of snow cover (Fang et al., 2019). For example, as time transits from thawing (freezing) seasons to freezing (thawing) seasons, the presence of snow cover could effectively reduce heat release from (heat absorption by) the soil surface and thus keep the soil surface warmer (colder) than the snow-free surfaces (Fang et al., 2019; Ling and Zhang, 2003; Stieglitz et al., 2003; Yang et al., 2008). The negative correlations between snow depth and SFD within the P_{solid}-controlled regions shown in Figs. 8b and 9c imply a primary warming effect of snow insulation over the TP. In supplementary Fig. S16, we compared the MODIS LST, simulated soil temperature at 5 cm deep ($T_{soil,\ 5cm}$), and observed $T_{soil,\ 5cm}$ during winter seasons at the CMA stations and find a close agreement between simulated and observed $T_{soil,\ 5cm}$, both of which are higher than the MODIS LST by ~1 °C when snow cover presents. However, such a discrepancy largely diminishes over snow-free surfaces Since MODIS LST measures the snow surface temperature over snow-covered surfaces, a higher $T_{soil,\ 5cm}$ than the MODIS LST further confirms the insulation effect of snow cover on the underlying soil surfaces over seasonally frozen ground in the TP.

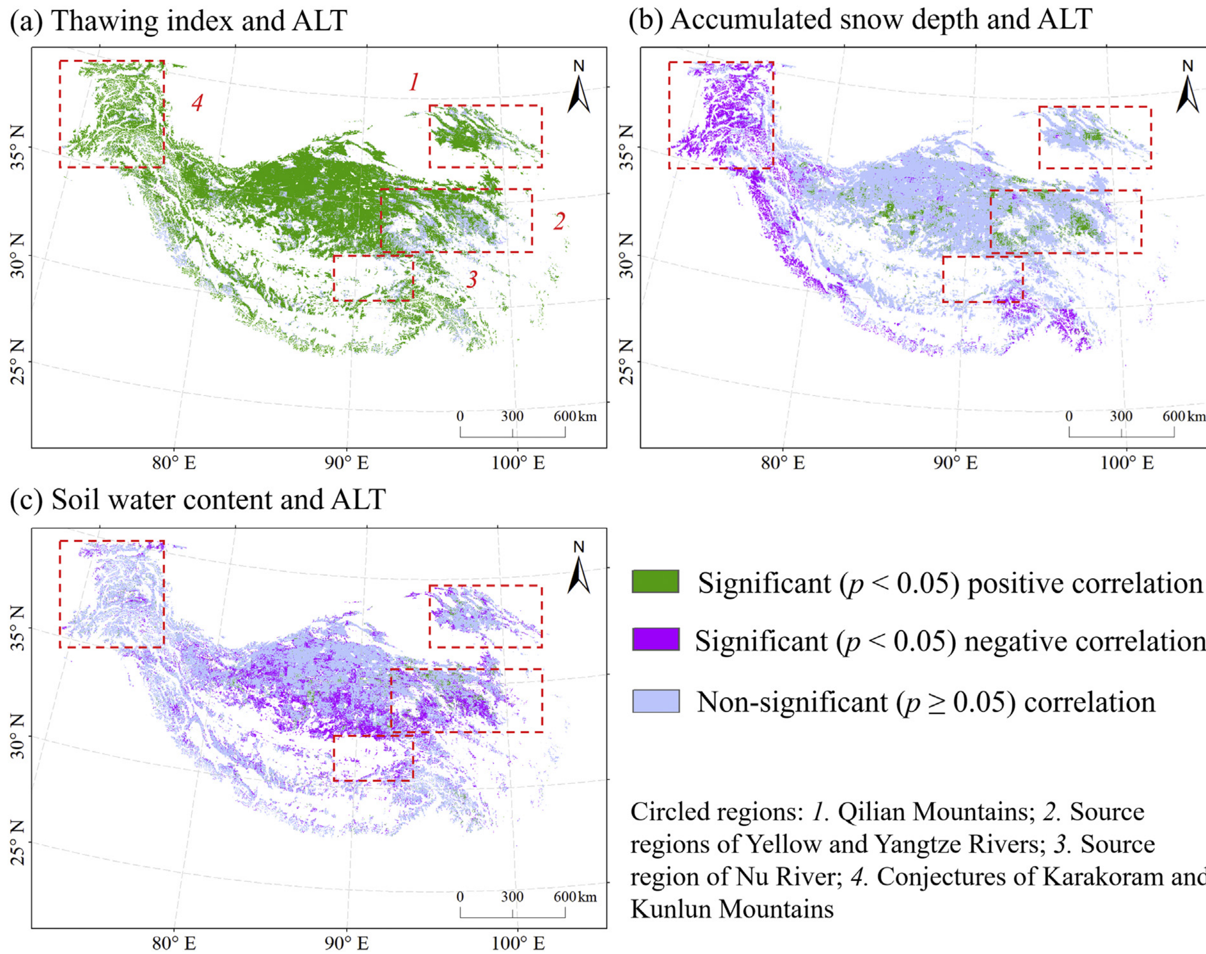

Fig. 10. Regions with significant ($p < .05$) and non-significant ($p \geq .05$) correlations between the temporal changes of annual maximum active layer thickness (ALT) and changes in (a) thawing index, (b) annually accumulated snow depth, and (c) annual mean soil water content (the sum of soil water in both liquid and soil phases within 0–5 m soil column) over permafrost.

In comparison, despite a nearly zero winter P_{liquid}, P_{liquid} in antecedent seasons could still show notable controls on SFD changes in arid regions of the southern plateau and the Qaidam Basin (Fig. 9d and e, and Supplementary Fig. S2). In arid regions, the relatively drier soil generally has a larger potential to hold infiltrated water and thus an abnormal large P_{liquid} may be stored long enough in the soil to exert impacts on SFD in the following freezing season (Liang et al., 2015). This may also explain the weak relationship between SFD and P_{liquid} in the high-latitude regions, where the climate is generally more humid than that of the TP (Frauenfeld and Zhang, 2011). Additionally, the replenishment of soil water through antecedent P_{liquid} could increase the phase-change heat and thermal conductivities, which respectively have a negative and a positive effect on the growth of SFD (Stefan, 1891). The phase-change heat steadily increases with soil water content, whereas the increase of soil thermal conductivity is much faster when the soil water content is low (smaller than ~0.2 $m^3\ m^{-3}$) and gradually slows down as soil water content increases (Tarnawski and Leong, 2000). As a result, the soil water content-induced phase-change effect could be weak in relatively dry regions but is likely to dominate over the thermal conductivity effect in more humid environments. This may partly explain the negative correlations between SFD and soil water content in the circled region 3 (relatively wet), and positive correlations in places between the circled regions 3 and 4 (relatively dry; Fig. 8c).

In terms of ALT, our results also suggest that P_{solid} and P_{liquid} exert impacts on the ALT temporal changes through their respective impacts on snow cover and soil water content (Figs. 10 and 11). However, different from SFD, the correlations between snow depth and ALT show different signs in P_{solid}-controlled regions (i.e., negative in the Nyainqntanglha Mountains and the Karakoram Mountains and positive in the source regions of the Yellow and Yangtze Rivers; Fig. 10b). This result implies different mechanisms in the control of ALT by P_{solid} in these two areas. For regions near the southern boundaries of the plateau (i.e., the Karakoram Mountains and Nyainqentanglha Mountains), the permafrost is mainly located on mountain tops with a long snow cover duration (> 6 months, Supplementary Fig. S17; also reported by Pu et al., 2007). The existence of snow cover insulates the atmospheric heating during the thawing season, which cools down the ground and leads to a negative snow depth-ALT correlation (Ling and Zhang, 2003). By contrast, in the central plateau (including the source regions of the Yellow and Yangtze Rivers), the thawing season is commonly free of snow and the snow cover during freezing seasons mainly warms the soil surface by preventing heat release from the soil layers (similar to the snow insulation effects on SFD changes), which prompts the growth of ALT (Wu et al., 2015). Consequently, a positive correlation between snow depth and ALT is found in these regions. Within the P_{liquid}-controlled area, P_{liquid} shows an overall increasing trend during the study period (Supplementary Fig. S12), which enhances infiltration that brings more heat from the near-surface to deeper layers near the thawing front and consequently prompts the growth of ALT. This result is consistent with observations by Wu et al. (2015) in these regions and by Hinkel et al. (2001) in Alaska, who reported that precipitation increase is mainly responsible for the rapid increase of ALT. However, since the permafrost degradation enhances the downward movement of

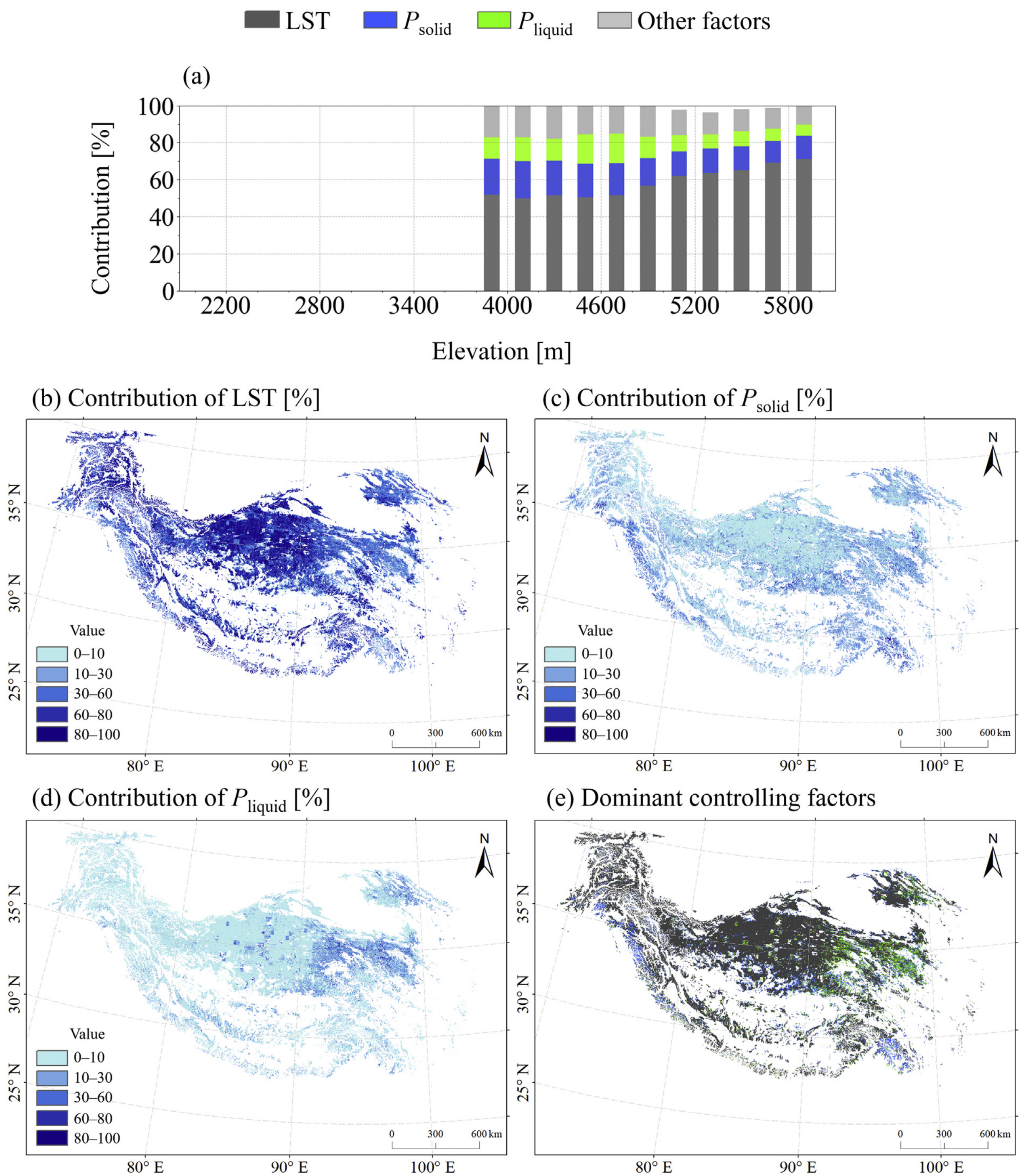

Fig. 11. Relative contributions of LST, P_{solid}, P_{liquid}, and other factors (sum of SWD, LWD, α, and NDVI) to the temporal changes of annual maximum active layer thickness (ALT) in permafrost regions. Part (a) shows the contributions of LST, black, P_{liquid}, P_{solid}, and other factors along the elevation gradient. Parts (b)–(d) show the spatial patterns of the relative contributions by LST, P_{solid}, and P_{liquid}, respectively. Part (e) shows the locations of dominant controlling factors.

near-surface liquid soil moisture to deeper layers (Cheng and Wu, 2007; Zhao et al., 2019), soil water content generally decreases in the top 5-m soil layer and increases in deeper layers (Supplementary Fig. S18), which partly explain the negative correlations between ALT and soil water content within the top 5-m soil column (Fig. 10c).

Apart from temperature and precipitation, the impacts of other factors on the control of spatial and temporal patterns of frozen soil are generally very small. Previous studies suggest that frozen soil simulations are also sensitive to changes in vegetation coverage (e.g., Li et al., 2019). On the one hand, enhanced vegetation growth under warming in temperature-limited regions induce a cooling effect that potentially impacts the underground freeze-thaw processes (Shen et al., 2015). On the other hand, changes in vegetation coverage directly affect soil water status and may consequently affect frozen soil status. Nevertheless, our results do not show a notable vegetation control on frozen soil patterns, partly because the cooling effect of vegetation greening has already been reflected in the observed LST in our model. Additionally, the impacts of vegetation change on soil water dynamics are unlikely to be significant, because the vegetation on the TP is generally thin and short with shallow roots, and the temporal trends in vegetation coverage are also generally small and non-significant (Supplementary Fig. S19) during the study period. It is thus not surprising that changes in NDVI only exert a very minor impact on frozen soil changes in our simulation (Supplementary Figs. S14 and S15).

Finally, there are also uncertainties and limitations associated with our study. First, the radiation-based MODIS LST were validated against the thermometer-based LST measurements at the CMA stations as done in several previous studies (e.g., Wu and Chen, 2005; Yang and Yang, 2006), since the ground-based measurements of upward longwave radiation were not available at these stations. Due to the probably large uncertainties of LST observations at the CMA stations (Liang, 2001) and the theoretical differences between the radiation-based and thermometer-based approaches in measuring LST (CMA, 2004; Wan and Dozier, 1996), some discrepancies (i.e., RMSE = 4.04 °C) existed between the two LST datasets (see Fig. S3). Second, despite the advantage of spatial consistency and temporal continuity, satellite-based forcings are found to have evident biases compared with ground observations (Langer et al., 2013; Ma et al., 2016). Such biases may be transferred to the simulated results and consequently lead to uncertainties in the model outputs (Langer et al., 2013). Here, we conduct an uncertainty analysis to investigate the impacts of biases in satellite data (i.e., LST, precipitation, SWD, LWD, and α) on the simulated SFD and ALT (Supplementary Text S2 and Fig. S20). We find that except for few regions near the boundaries between permafrost and seasonally frozen ground, the impacts associated with the uncertainties are generally small. Averaged over the entire TP, biases in LST (−0.26 °C), precipitation (+6.17 mm month^{-1}), SWD (−21 W m^{-2}), LWD (+5 W m^{-2}), and α (−0.01) lead to a change in simulated SFD by +0.08 m, −0.01 m, +0.01 m, 0.0 m, and − 0.01 m, and a change in simulated ALT by −0.08 m, 0.0 m, 0.0 m, 0.0 m, and 0.0 m, respectively. Third, the geothermal flux is estimated from the deep-ground T_{soil} measurements at limited boreholes (mainly along the highway/railways in the central plateau; Cao et al., 2019; Ran et al., 2018), which may result in uncertainties in the lower boundary conditions, especially for the western and southern plateau where the observation of T_{soil} is extremely rare (Shi et al., 2018). The uncertain lower boundary condition may also partly account for the increasing cold bias along depth in our T_{soil} simulation at CMA stations (Table 2). Forth, the TP is characterized as a mountainous frozen soil region, where the topography and landscape show great spatial variabilities (Zhao and Li, 2015). Since the CMA stations are mainly located in mountain valleys where the surface properties are likely to vary substantially within one MODIS pixel (i.e., ~1 × 1 km), it may partly explain the difference between modelled and observed T_{soil} (D_f) at the CMA stations. In addition, despite an overall good performance of our model in identifying the frozen ground types, the uncertainties are especially evident near the lower limit of permafrost (roughly within 2 km), where frozen ground types may vary greatly within a short distance (< 1 km) (e.g., Wu et al., 2017). In such regions, accurate discrimination of frozen ground types requires data at much finer spatial resolutions (Luo et al., 2019). Last but not least, in the attribution of temporal frozen soil changes, the experimental design (by examining the difference between modelling experiments) could not fully capture the nonlinear interactions among climatic factors (Mao et al., 2015; Zhu et al., 2016). As a result, the sum of our estimated contributions of climatic factors is generally less than 100% (Figs. 9 and 11). All these issues need to be addressed to further improve our understanding of the spatiotemporal changes of frozen soil and the driving mechanisms over the TP in future studies.

6. Conclusion

In this study, a process-based, satellite-driven model (GBEHM-RS) is employed for frozen soil simulation at an unprecedented high spatial resolution (1 × 1 km) over the TP region with complex climate, topography, and landscape conditions. Following comprehensive model validations, the spatial and temporal patterns of frozen soil during 2002–2016 are quantified and the driving mechanisms are investigated. Major conclusions are summarized below:

1) Validated against observations at 608 boreholes, GBEHM-RS has obtained a reasonable performance in identifying the locations of seasonally frozen ground (at ~86.3% boreholes) and permafrost (at ~79.1% boreholes). Moreover, in both seasonally frozen ground and permafrost, GBEHM-RS satisfactorily captures the spatial pattern and temporal changes of ground thermal regimes against measured T_{soil} and D_f at 109 CMA stations ($T_{soil}R^2$ ranges between 0.84 and 0.91, mean bias ranges between −0.36 °C and −0.27 °C, and RMSE ranges between 1.61 °C and 3.25 °C at eight depths, and D_fR^2 = 0.65, mean bias = +0.04 m, and RMSE = 0.35 m), MAGT at 150 permafrost boreholes (R^2 = 0.65, mean bias = +0.49 °C, RMSE = 0.72 °C), ALT at 76 permafrost boreholes (R^2 = 0.58, mean bias = −0.1 m, and RMSE = 0.69 m), and deep-ground T_{soil} profiles at four GTN-P boreholes (with mean biases within ± 1.0 °C from 0 m to over 40 m deep).

2) Over the entire TP, the seasonally frozen ground and permafrost respectively occupy an area of 1.83 (~56%) and 1.22 (~37%) million km^2. The permafrost is primarily located on the northern and western plateau with a higher elevation and larger soil ice content (> 400 kg m^{-2} within 0–5 m soil column), whereas the seasonally frozen ground is mainly distributed across the southern and eastern plateau where elevations are relatively low. The plateau-averaged SFD (ALT) is 1.29 (1.85) m and its spatial patterns are mainly controlled by the LST during the freezing (thawing) season. However, the influences of LST during antecedent seasons on frozen soils (i.e., thawing index for SFD and freezing index for ALT) gradually increase as regions moving towards the boundaries between the permafrost and seasonally frozen ground, leading to much larger magnitudes and higher spatial variabilities of SFD and ALT (> 5 m) than other regions.

3) During 2002–2016, ALT shows an overwhelmingly increasing trend across the plateau at an average rate of +3.17 cm yr^{-1}, and SFD exhibits both increasing (at ~38% areas) and decreasing trends (at ~62% areas) across the plateau. The differences between the temporal changes of SFD and ALT are mainly caused by the asymmetric warming trends during the freezing and thawing seasons. In addition, P_{liquid} is found to impact on the temporal changes of SFD, especially in arid regions (e.g., the Qaidam Basin and the southern plateau), and both P_{liquid} and P_{solid} show notable impacts on the temporal changes of ALT, especially in the source regions of the Yangtze and Yellow Rivers.

To conclude, our study demonstrates the validity and advantages of the satellite-based method in frozen soil simulations over large scales with complex topography and landscapes and emphasizes the importance of both temperature and precipitation in the control of frozen soil changes. The modelled frozen soil maps are process-based, well-validated estimates, when combined with other estimates using different methods/model inputs, may help us to achieve a more robust quantification and a greater understanding of the spatial and temporal patterns of frozen soil in the TP.

Acknowledgments

This research was supported by grants from the National Natural Science Foundation of China (Grant No. 41630856 and 41890821). Y. Yang acknowledges support from the Department of Science and Technology, Qinghai, China (Grant No. 2019-SF-A4). D. Chen acknowledges supported by the Strategic Priority Research Program of Chinese Academy of Sciences (XDA20060401) and the Swedish VR (2017-03780). We thank Jingfeng Wang at Georgia Institute of Technology, Hong-yi Li at the University of Houston, and Hongyi Li, Fujun Niu, and Tonghua Wu at Chinese Academy of Science for providing supports on this work. The authors also thank Editor Dr. Marie

Weiss and five anonymous reviewers for their very constructive comments. The China Meteorological Administration is acknowledged for providing the in situ observations of T_{soil}, frozen depths, LST, and precipitation (http://data.cma.cn/). The in situ observations of SWD, LWD, and α at the CAMP-Tibet stations were available at https://archive.eol.ucar.edu/projects/ceop/dm/insitu/sites/ceop_ap/Tibet/ANNI-AWS.

The MODIS land surface temperature and vegetation data were retrieved from the online Data Pool, courtesy of the NASA Land Processes Distributed Active Archive Center (LP DAAC), USGS/Earth Resources Observation and Science (EROS) Center, Sioux Falls, South Dakota, https://lpdaac.usgs.gov/data_access/data_pool. The AIRX3STD land surface temperature and meteorological data (including the cloud fraction, air temperature, relative humidity, and air pressure) were retrieved from https://earthdata.nasa.gov/about/daacs/daac-ges-disc. The TRMM 3B42 V7 precipitation product was retrieved from https://pmm.nasa.gov/data-access/downloads/trmm. The 'The Soil Database of China for Land Surface Modelling' and 'A Global Depth to Bedrock Dataset for Earth System Modeling' were retrieved from http://globalchange.bnu.edu.cn. The MODIS gap-filled surface albedo was retrieved from ftp://rsftp.eeos.umb.edu/data02/Gapfilled/. We also took advantage of the computational platform maintained by the National Supercomputer Centre in Guangzhou. Finally, a portion of this research was carried out at the Jet Propulsion Laboratory, California Institute of Technology, under contract with NASA.

Declaration of interests

The authors declare that they have no known competing financial interests or personal relationships that could have appeared to influence the work reported in this paper.

Appendix A. Evaluation criteria, i.e., mean bias, root-mean-square error (RMSE), and coefficient of determination (or multiple correlation coefficient, R^2), are calculated as

$$\text{mean bias} = \frac{1}{N}\cdot\sum_{i=1}^{N}(\text{Sim}_i - \text{Obs}_i) \tag{A1}$$

$$\text{RMSE} = \sqrt{\frac{\sum_{i=1}^{N}(\text{Sim}_i - \text{Obs}_i)^2}{N}} \tag{A2}$$

$$R^2 = \frac{\sum_{i=1}^{N}(\text{Obs}_i - \overline{\text{Obs}})\cdot(\text{Sim}_i - \overline{\text{Sim}})}{\sqrt{\sum_{i=1}^{N}(\text{Obs}_i - \overline{\text{Obs}})^2}\cdot\sqrt{\sum_{i=1}^{N}(\text{Sim}_i - \overline{\text{Sim}})^2}} \tag{A3}$$

where 'Sim' denotes simulated results, 'Obs' denotes ground observations, N is the size of a data sequence, i indicates the data order, $\overline{x}$ is the average value of x.

Appendix A. Supplementary data

Supplementary data to this article can be found online at https://doi.org/10.1016/j.rse.2020.111927.

References

Anderson, E., 1976. A point energy and mass balance model of a snow cover. In: NOAA Technical Report NWS 19. Office of Hydrology, National Weather Service, Silver Spring, MD.
Bartelt, P., Lehning, M., 2002. A physical snowpack model for the swiss avalanche warning: part I: numerical model, cold Reg. Sci. Technol. 35, 123–145.
Baumann, F., He, J., Schmidt, K., Kühn, P., Scholten, T., 2009. Pedogenesis, permafrost, and soil moisture as controlling factors for soil nitrogen and carbon contents across the Tibetan plateau. Glob. Chang. Biol. 15 (12), 3001–3017.
Bianchini, S., Raspini, F., Solari, L., et al., 2018. From picture to movie: twenty years of ground deformation recording over Tuscany region (Italy) with satellite InSAR. Front. Earth Sci. 6, 177.
Biskaborn, B., Smith, S., Noetzli, J., et al., 2019. Permafrost is warming at a global scale. Nat. Commun. 10 (1), 264.
Breiman, L., 2001. Random forests. Mach. Learn. 45 (1), 5–32.
Brucker, L., Dinnat, E., Koenig, L., 2014. Weekly gridded Aquarius L-band radiometer/scatterometer observations and salinity retrievals over the polar regions—part 1: product description. Cryosphere 8, 905–913.
Cao, B., Zhang, T., Wu, Q., Sheng, Y., Zhao, L., Zou, D., 2019. Brief communication: evaluation and inter-comparisons of Qinghai–Tibet plateau permafrost maps based on a new inventory of field evidence. Cryosphere. 13 (2), 511–519.
Cheng, G., Wu, T., 2007. Responses of permafrost to climate change and their environmental significance, Qinghai-Tibet Plateau. J. Geophy. Res. Earth 12, 1–10 (112.F2).
CMA, 2004. Specifications for Surface Meteorological Observation. China Meteorological Press, Beijing, China, pp. 82–88 (in Chinese).
Dai, Y., Zeng, Q., 1997. A land surface model (IAP94) for climate studies. Part I: formulation and validation in off-line experiments. Adv. Atmos. Sci. 14, 433–460.
Ding, Y., Zhang, S., Zhao, L., Li, Z., Kang, S., 2019. Global warming weakening the inherent stability of glaciers and permafrost. Sci. B. 64 (4), 245–253.
Fang, X., Luo, S., Lyu, S., 2019. Observed soil temperature trends associated with climate change in the Tibetan plateau, 1960–2014. Theor. Appl. Climatol. 135 (1–2), 169–181.
Feng, Y., Liang, S., Kuang, X., Wang, G., Wang, X., Wu, P., Wan, L., Wu, Q., 2019. Effect of climate and thaw depth on alpine vegetation variations at different permafrost degrading stages in the Tibetan plateau, China. Arct. Antarct. Alp. Res. 51 (1), 155–172. https://doi.org/10.1080/15230430.2019.1605798.
Flerchinger, G., Saxton, K., 1989. Simultaneous heat and water model of a freezing snow-residue-soil system: I. theory and development. T. ASAE 32, 565–571. https://doi.org/10.13031/2013.31040.
Frauenfeld, O., Zhang, T., 2011. An observational 71-year history of seasonally frozen ground changes in the Eurasian high latitudes. Environ. Res. Lett. 6 (4), 044024.
Gao, B., Yang, D., Qin, Y., Wang, Y., Li, H., Zhang, Y., Zhang, T., 2018. Change in frozen soils and its effect on regional hydrology, upper Heihe basin, northeastern Qinghai–Tibetan plateau. Cryosphere 12, 657–673. https://doi.org/10.5194/tc-12-657-2018.
Grosse, G., Goetz, S., McGuire, A., Romanvosky, V., Schuur, E., 2016. Changing permafrost in a warming world and feedbacks to the earth system. Environ. Res. Lett. 11 (4), 040201.
Guo, D., Sun, J., Yang, K., et al., 2019. Satellite data reveal southwestern Tibetan plateau cooling since 2001 due to snow-albedo feedback. Int. J. Climatol. 1–12.
Guo, D., Sun, J., Li, H., et al., 2020. Attribution of historical near-surface permafrost degradation to anthropogenic greenhouse gas warming. Environ. Res. Lett.
Hardy, J., Groffman, P., Fitzhugh, R., Hnery, K., Welman, A., Demers, J., Fashey, T., Driscoll, C., Tierney, G., Nolan, S., 2001. Snow depth manipulation and its influence on soil frost and water dynamics in a northern hardwood forest. Biogeochemistry 56 (2), 151–174.
Hinkel, K., Paetzold, F., Nelson, F., 2001. Patterns of soil temperature and moisture in the active layer and upper permafrost at Barrow, Alaska: 1993–1999. Glob. Planet. Chang. 29 (3–4), 293–309.
Jin, H., He, R., Cheng, C., et al., 2009. Changes in frozen ground in the source area of the Yellow River on the Qinghai–Tibet plateau, China, and their eco-environmental impacts. Environ. Res. Lett. 4 (4), 045206.
Jin, H., Luo, D., Wang, S., Lü, L., Wu, J., 2011. Spatiotemporal variability of permafrost degradation on the Qinghai-Tibet plateau. Sci. Cold Arid. Reg. 3, 281–305.

Jordan, R., 1991. A One-Dimensional Temperature Model for a Snow Cover, Technical Documentation for SNTHERM.89. Cold Regions Research and Engineering Lab, Hanover NH (49 pp).
Kane, D., Hinkel, K., Goering, D., Hinzman, L., Outcalt, S., 2002. Non-conductive heat transfer associated with frozen soils. Glob. Planet. Chang. 29 (3–4), 275–292.
Karjalainen, O., Luoto, M., Aalto, J., Hjort, J., 2019. New insights into the environmental factors controlling the ground thermal regime across the northern hemisphere. Cryosphere 13, 693–707.
Kim, Y., Kimball, J., Glassy, J., Du, J., 2017. An extended global earth system data record on daily landscape freeze–thaw status determined from satellite passive microwave remote sensing. Earth Syst. Sci. Data 9, 133.
Langer, M., Westermann, S., Heikenfeld, M., Dorn, W., Boike, J., 2013. Satellite-based modeling of permafrost temperatures in a tundra lowland landscape. Remote Sens. Environ. 135, 12–24. https://doi.org/10.1016/j.rse.2013.03.011.
Li, Z., Zhao, R., Hu, J., et al., 2015. InSAR analysis of surface deformation over permafrost to estimate active layer thickness based on one-dimensional heat transfer model of soils. Sci. Rep. 5, 15542.
Li, C., Lu, H., Leung, L., et al., 2019. Improving land surface temperature simulation in CoLM over the Tibetan plateau through fractional vegetation cover derived from a remotely sensed clumping index and model-simulated leaf area index. J. Geophys. Res.-Atmos. 124 (5), 2620–2642.
Liang, S., 2001. Irregular installation and error analysis of ground temperature thermometer and curved pipe ground temperature thermometer. Shandong Meteorol. 21, 83 (in Chinese).
Liang, W., Yang, Y., Fan, D., et al., 2015. Analysis of spatial and temporal patterns of net primary production and their climate controls in China from 1982 to 2010. Agric. For. Meteorol. 204, 22–36.
Ling, F., Zhang, T., 2003. Impact of the timing and duration of seasonal snow cover on the active layer and permafrost in the Alaskan Arctic. Permafrost Periglac. 14 (2), 141–150.
Liu, J., 2015. Reconstruction of the Past Ground Surface Temperature Changes Using Borehole Paleothermometry. Lanzhou University, China.
Liu, G., Wang, W., Zhao, L., et al., 2015. Using transient electromagnetic method to sound permafrost depth in the west Kunlun Mountains. J. Glaciol. Geocryol. 37 (1), 48 (in Chinese with English abstract).
Lu, Q., Zhao, D., Wu, S., 2017. Simulated responses of permafrost distribution to climate change on the Qinghai–Tibet plateau. Sci. Rep. 7 (1), 3845.
Luo, D., Jin, H., Lin, L., He, R., Yang, S., Chang, X., 2012a. Degradation of permafrost and cold-environments on the interior and eastern Qinghai plateau. J. Glaciol. Geocryol. 34, 538–546.
Luo, D., Jin, H., Lin, L., He, R., Yang, S., Chang, X., 2012b. New progress on permafrost temperature and thickness in the source area of the Huanghe river. Sci. Geogr. Sin. 32, 898–904 (in Chinese with English abstract).
Luo, D., Jin, H., Wu, Q., Bense, V., He, R., Ma, Q., Gao, S., Jin, X., Lv, L., 2018. Thermal regime of warm-dry permafrost in relation to ground surface temperature in the source areas of the Yangtze and yellow rivers on the Qinghai-Tibet plateau, SW China. Sci. Total Environ. 618, 1033–1045.
Luo, J., Yin, G., Niu, F., Lin, Z., Liu, M., 2019. High spatial resolution modeling of climate change impacts on permafrost thermal conditions for the Beiluhe basin, Qinghai-Tibet Plateau. Remote Sens. 11, 1–16.
Luthin, J., Guymon, G., 1974. Soil moisture-vegetation-temperature relationships in Central Alaska. J. Hydrol. 23 (3–4), 233–246.
Lyu, H., McColl, K., Li, X., et al., 2018. Validation of the SMAP freeze/thaw product using categorical triple collocation. Remote Sens. Environ. 205, 329–337.
Ma, Y., Tang, G., Long, D., Yong, B., Zhong, L., Wan, W., Hong, Y., 2016. Similarity and error intercomparison of the GPM and its predecessor-TRMM multisatellite precipitation analysis using the best available hourly gauge network over the Tibetan plateau. Remote Sens. 8 (7), 569.
Mao, J., Fu, W., Shi, X., et al., 2015. Disentangling climatic and anthropogenic controls on global terrestrial evapotranspiration trends. Environ. Res. Lett. 10 (9), 094008.
Obu, J., Westermann, S., Bartsch, A., et al., 2019. Northern hemisphere permafrost map based on TTOP modelling for 2000–2016 at 1 km2 scale. Earth-Sci. Rev. 193, 299–316.
Pang, Q., Li, S., Wu, T., et al., 2006. Simulated distribution of active layer depths in the frozen ground regions of Tibetan plateau. J. Glaciol. Geocryol. 3 (in Chinese with English abstract).
Park, H., Walsh, J., Fedorov, A., et al., 2013. The influence of climate and hydrological variables on opposite anomaly in active-layer thickness between Eurasian and north American watersheds. Cryosphere. 7 (2).
Peng, X., Zhang, T., Frauenfeld, O., et al., 2017. Response of seasonal soil freeze depth to climate change across China. Cryosphere 11, 3.
Peng, X., Zhang, T., Frauenfeld, O.W., et al., 2018. Spatiotemporal changes in active layer thickness under contemporary and projected climate in the northern hemisphere. J. Clim. 31 (1), 251–266.
Pu, Z., Li, X., Salomonson, V., 2007. MODIS/Terra observed seasonal variations of snow cover over the Tibetan Plateau. Geophys. Res. Lett. 34, 1–6 (34.6).
Qiao, Y., Zhao, L., Pang, Q., Chen, J., Gao, Z., 2015. Characteristics of permafrost in Gerze County on the Tibetan plateau. J. Glaciol. Geocryol. 37 (6), 145–1460 (in Chinese with English abstract).
Qin, Y., Wu, T., Zhao, L., Wu, X., Li, R., Xie, C., Pang, Q., Hu, G., Qiao, Y., Zhao, G., Liu, G., Zhu, X., Hao, J., 2017. Numerical modeling of the active layer thickness and permafrost thermal state across Qinghai-Tibetan plateau. J. Geophy. Res. Atmos. 122 (11), 604–11,620.
Ran, Y., Li, X., 2019. Progress, challenges and opportunities of permafrost mapping in China. Adv. Earth Science 34 (10), 1015–1027 (in Chinese with English abstract).
Ran, Y., Li, X., Cheng, G., 2018. Climate warming over the past half century has led to thermal degradation of permafrost on the Qinghai–Tibet plateau. Cryosphere 12, 595–608.
Rautiainen, K., Parkkinen, T., Lemmetynien, J., et al., 2016. SMOS prototype algorithm for detecting autumn soil freezing. Remote Sens. Environ. 180, 346–360.
Roy, A., Royer, A., Derksen, C., Brucker, L., Langlois, A., Mialon, A., Kerr, Y., 2015. Evaluation of spaceborne L-band radiometer measurements for terrestrial freeze/thaw retrievals in Canada. IEEE J. Sel. Top. Appl. 8, 4442–4459.
Shi, Y., Niu, F., Yang, C., et al., 2018. Permafrost presence/absence mapping of the Qinghai-Tibet plateau based on multi-source remote sensing data. Remote Sens. 10 (2), 309.
Shur, Y., Jorgenson, M., 2007. Patterns of permafrost formation and degradation in relation to climate and ecosystem. Permafrost Periglac. 18 (1), 7–19.
Slater, A., Pitman, A., Desborough, C., 1998. Simulation of freeze-thaw cycles in a general circulation model land surface scheme. J. Geophys. Res.-Atmos. 11303–11312 103.D10.
Smith, M., Riseborough, D., 2002. Climate and the limits of permafrost: a zonal analysis. Permafrost Periglac. 13 (1), 1–15.
Stefan, J., 1891. Über die Theorie der Eisbildung, insbesondere über die Eisbildung im Polarmeere. Ann. Phys. 278 (2), 269–286.
Stieglitz, M., Déry, S., Romanovsky, V., et al., 2003. The role of snow cover in the warming of arctic permafrost. Geophys. Res. Lett. 30 (13).
Su, F., Duan, X., Chen, D., Hao, Z., Lan, C., 2013. Evaluation of the global climate models in the CMIP5 over the Tibetan plateau. J. Clim. 26, 3187–3208.
Tarnawski, V.R., Leong, W.H., 2000. Thermal conductivity of soils at very low moisture content and moderate temperatures. Transport Porous Med. 41, 137–147.
Tong, K., Su, F., Yang, D., Hao, Z., 2014. Evaluation of satellite precipitation retrievals and their potential utilities in hydrologic modeling over the Tibetan plateau. J. Hydrol. 519, 423–437.
van Everdigen, R., 1998. Multi-language glossary of permafrost and related groundice terms. Definitions 78.
Wan, Z., Dozier, J., 1996. A generalized split-window algorithm for retrieving land-surface temperature from space. IEEE T. Geosci. Remote. 16, 892–905.
Wang, S., 1990. Discussions on the en-permafrost water. Hydrogeol. Eng. Geol. 19 (1), 46–47 (in Chinese with English abstract).
Wang, T., Wang, N., Li, S., 2006. Map of the Glaciers, Frozen Ground and Desert in China, 1:4,000,000. Chinese Map Press, Beijing, China.
Wang, G., Hu, H., Li, T., 2009. The influence of freeze–thaw cycles of active soil layer on surface runoff in a permafrost watershed. J. Hydrol. 375 (3-4), 438–449.
Wang, T., Yang, D., Fang, B., Yang, W., Qin, Y., Wang, Y., 2019a. Data-driven mapping of the spatial distribution and potential changes of frozen ground over the Tibetan plateau. Sci. Total Environ. 649, 515–525.
Wang, T., Wu, T., Wang, P., Li, R., Xie, C., Zou, D., 2019b. Spatial distribution and changes of permafrost on the Qinghai-Tibet plateau revealed by statistical models during the period of 1980 to 2010. Sci. Total Environ. 650, 661–670.
Wen, Z., Niu, F., Yu, Q., et al., 2014. The role of rainfall in the thermal-moisture dynamics of the active layer at Beiluhe of Qinghai-Tibetan plateau. Environ. Earth Sci. 71 (3), 1195–1204.
Westermann, S., Østby, T., Gisnås, K., Schuler, T., Etzelmüller, B., 2015. A ground temperature map of the North Atlantic permafrost region based on remote sensing and reanalysis data. Cryosphere. 9 (3), 1303–1319.
Westermann, S., Langer, M., Boike, J., Heikenfeld, M., Peter, M., Etzelmüller, B., Krinner, G., 2016. Simulating the thermal regime and thaw processes of ice-rich permafrost ground with the land-surface model CryoGrid 3. Geosci. Model Devel. Dis. 9, 523–546.
Wu, X., Chen, W., 2005. Land surface temperature estimated by remote sensing data from FY-1D polar meteorological satellite. J. Appl. Meteorol. Sci. 16 (1), 45–53.
Wu, Q., Zhang, T., 2008. Recent permafrost warming on the Qinghai-Tibetan Plateau. J. Geophy. Res.-Atmos. 113, 1–22 (113.D13).
Wu, Q., Zhang, T., 2010. Changes in active layer thickness over the Qinghai-Tibetan Plateau from 1995 to 2007. J. Geophy. Res. Atmos. 72, 32–38 (115.D9).
Wu, Q., Zhang, T., Liu, Y., 2010. Permafrost temperatures and thickness on the Qinghai-Tibet plateau. Glob. Planet. Chang. 72 (1–2), 32–38.
Wu, T., Zhao, L., Li, R., Wang, Q., Xie, C., Peng, Q., 2013. Recent ground surface warming and its effects on permafrost on the Central Qinghai-Tibet plateau. Int. J. Climatol. 33 (4), 920–930.
Wu, Q., Hou, Y., Yun, H., Liu, Y., 2015. Changes in active-layer thickness and near-surface permafrost between 2002 and 2012 in alpine ecosystems, Qinghai–Xizang (Tibet) plateau, China. Glob. Planet. Chang. 124, 149–155.
Wu, Q., Yu, W., Jin, H., 2017. No protection of permafrost due to desertification on the Qinghai–Tibet plateau. Sci. Rep. 7 (1), 1–8.
Wu, X., Nan, Z., Zhao, S., Zhao, L., Cheng, G., 2018. Spatial modeling of permafrost distribution and properties on the Qinghai-Tibet plateau. Permafrost Periglac. 29 (2), 86–99.
Xie, C., Zhao, L., Wu, T., et al., 2012. Changes in the thermal and hydraulic regime within the active layer in the Qinghai-Tibet plateau. J. Mt. Sci. 9 (4), 483–491.
Xie, C., William, G., Zhao, L., et al., 2015. Temperature-dependent adjustments of the permafrost thermal profiles on the Qinghai-Tibet plateau, China. Arct. Antarct. Alp. Res. 47 (4), 719–728.
Yang, H., Yang, Z., 2006. A modified land surface temperature split window retrieval algorithm and its applications over China. Global planet. Chang. 52 (1–4), 207–215 (in Chinese with English abstrct).
Yang, M., Yao, T., Nelson, F., Shiklomanov, N., Guo, D., Wang, C., 2008. Snow cover and depth of freeze-thaw on the Tibetan plateau: a case study from 1997 to 1998. Phys. Geogr. 29 (3), 208–221. https://doi.org/10.2747/0272-3646.29.3.208.
Yang, D., Gao, B., Jiao, Y., Lei, H., Zhang, Y., Yang, H., Cong, Z., 2015. A distributed scheme developed for eco-hydrological modeling in the upper Heihe river. Sci. China

Earth Sci. 58, 36–45. https://doi.org/10.1007/s11430-014-5029-7.
Yi, Y., Kimball, J., Chen, R., Moghaddam, M., et al., 2018. Characterizing permafrost active layer dynamics and sensitivity to landscape spatial heterogeneity in Alaska. Cryosphere. 12, 145–161. https://doi.org/10.5194/tc-12-145-2018.
Yi, Y., Kimball, J., Chen, R., Moghaddam, M., Miller, C., 2019. Sensitivity of active-layer freezing process to snow cover in Arctic Alaska. Cryosphere. 13, 197–218. https://doi.org/10.5194/tc-13-197-2019.
Yin, G., Niu, F., Lin, Z., Luo, J., Liu, M., 2017. Effects of local factors and climate on permafrost conditions and distribution in Beiluhe basin, Qinghai-Tibet plateau, China. Sci. Total Environ. 581, 472–485.
Zhang, T., 2005. Influence of the seasonal snow cover on the ground thermal regime: an overview. Rev. Geophys. 43, 4.
Zhang, T., Barry, R., Knowles, K., Heginbottom, J., Brown, J., 1999. Statistics and characteristics of permafrost and ground-ice distribution in the northern hemisphere. Polar Geogr. 23, 132–154.
Zhang, S., Wang, Y., Zhao, Y., Huang, Y., Li, Y.G., Shi, W.D., Shang, X.G., 2004. Permafrost degradation and its environmental sequent in the source regions of the yellow river. J. Glaciol. Geocryol. 26, 1–6 (in Chinese with English abstract).
Zhang, T., Frauenfeld, O., Serreze, M., et al., 2005. Spatial and temporal variability in active layer thickness over the Russian Arctic drainage basin. J. Geophys. Res.-Atmos. 110, D16.
Zhao, W., Li, A., 2015. A review on land surface processes modelling over complex terrain. Adv. Meteorol. 2015.
Zhao, L., Hu, G., Zou, D., et al., 2019. Permafrost changes and its effects on hydrological processes on Qinghai-Tibet plateau. B. Chin. A. Sci. 34 (11), 1233–1245 (in Chinese with English abstract).
Zheng, G., Yang, Y., Yang, D., Dafflon, B., Lei, H., Yang, H., 2019. Satellite-based simulation of soil freezing/thawing processes in the northeast Tibetan plateau. Remote Sens. Environ. 231, 111269.
Zhong, L., Ma, Y., Salama, M., et al., 2010. Assessment of vegetation dynamics and their response to variations in precipitation and temperature in the Tibetan plateau. Clim. Chang. 103 (3–4), 519–535.
Zhou, Y., Qiu, G., Guo, D., Li, S., 2000. Frozen Ground in China. Science Press, Beijing, pp. 128–136 (in Chinese).
Zhou, S., Yu, B., Schwalm, C.R., et al., 2017. Response of water use efficiency to global environmental change based on output from terrestrial biosphere models. Global Biogeochem. Cy. 31, 1639–1655.
Zhu, Z., Piao, S., Myneni, R., et al., 2016. Greening of the earth and its drivers. Nat. Clim. Chang. 6 (8), 791.
Zou, D., Zhao, L., Sheng, Y., Chen, J., Hu, G., Wu, T., Wu, J., Xie, C., Wu, X., Pang, Q., Wang, W., Du, E., Li, W., Liu, G., Li, J., Qin, Y., Qiao, Y., Wang, Z., Shi, J., Cheng, G., 2017. A new map of permafrost distribution on the Tibetan plateau. Cryosphere 11, 2527–2542. https://doi.org/10.5194/tc-11-2527-2017.